

Influence of energy dissipation at the interphase boundaries on impact fracture behaviour of a plain carbon steel

S.V.Panin^{ab}D.D.Moiseenko^aP.V.Maksimov^aI.V.Vlasov^{ab}A.V.Byakov^{ab}P.O.Maruschak^cF.Berto^dS.Schmauder^e
A.Vinogradov^d

<https://doi.org/10.1016/j.tafmec.2017.09.010>Get rights and content

Abstract

The paper deals with the impact deformation and fracture behaviour of commercial plain carbon pipe steel 17Mn1Si. The explicit account of the internal grain structure, temperature and geometry of the notch have been made in theoretical physical mesomechanics formulation aiming at in depth understanding of the role of strain energy factors in dynamic fracture. Theoretical method of excitable cellular automata and laboratory impact bending tests followed by fractographic analysis were paired with time–frequency analysis of acoustic emission accompanying local deformation and fracture processes. It was shown that formulation of the crack opening criterion under dynamic loading conditions should explicitly account for rotation energy accumulation and incorporate the microscopic temporal and spatial details of defect generation from internal (grain) boundaries. A fairly good agreement has been found between the strain energy characteristics obtained from mechanical loading data and independently measured acoustic emission signal being distinguished in terms of consumed and released energy. The impact toughness almost linearly decreased with temperature, which was consistent with fractographic observations. At the stage of crack initiation, when the energy dissipation processes at the internal structure elements significantly affect the initiation of dynamic fracture, the acoustic emission energy reduced in proportion to the expended mechanical energy, which considerably decreased with temperature. The vital role of the energy release at interface/grain boundaries and its decreased significance with decreasing temperature was demonstrated both in numeric simulations and in dynamic experiments.

1. Introduction

The rational understanding of the [deformation](#) behaviour of structurally inhomogeneous materials within the framework of physical mesomechanics [\[1\]](#) involves formulating of hierarchical models accounting for interaction of [deformation processes](#) occurring in the material at different scales. Special care is given to [characterization](#) of the [local response](#) at the [mesoscale](#) level, where the stress-strain state is not distributed evenly

within a plastically deforming solid. The mesoscale involves into consideration a [large number](#) of existing interfaces and strain-induced defects, their nucleation and development [\[2\]](#), [\[3\]](#), [\[4\]](#), [\[5\]](#), [\[6\]](#), [\[7\]](#), [\[8\]](#). [Plastic flow](#) processes associated with initiation and storage of defects and discontinuities are initiated close to structural [inhomogeneities](#) [\[9\]](#), [\[10\]](#), [\[11\]](#). A [surface layer](#), where [plastic deformation](#) processes develop first, is considered as an additional structural level of deformation [\[12\]](#), [\[13\]](#), [\[14\]](#), [\[15\]](#), [\[16\]](#), [\[17\]](#). The [non-linearity](#) of the latter may be taken into account by considering the independent 2D-subsystem (surface and interface boundaries) and 3D-crystal [subsystem](#) (inside the grain body) [\[1\]](#).

The ductility and [fracture toughness](#) of [pipe steels](#) is heavily dependent on the [microstructure](#) where the distribution of phases and grain sizes plays a key role [\[18\]](#), [\[19\]](#), [\[20\]](#), [\[21\]](#), [\[22\]](#). In the case of brittle and/or mixed fracture, [micro-cracks](#) initiate primarily at the [grain boundaries](#). Thus, the optimization of the grain size distribution and the comprehensive understanding of the mechanical behaviour of [individual grains](#) and their agglomerates under dynamic [impact loading](#) [\[23\]](#), [\[24\]](#) is of significant importance. Field [pneumatic tests](#) yielded that the ability to terminate the extended [ductile fracture](#) is determined by the amount and intensity of the [plastic strain](#) of the metal at the tip of the [propagating crack](#) [\[25\]](#), [\[26\]](#), [\[27\]](#). At the stage of stable ductile [crack growth](#), the size of the [plastic zone](#) at its tip is directly related to the size of the material [structural elements](#) (in our case, the ferritic and pearlitic grains). The more material around the propagating [crack tip](#) is involved in the [fracture resistance](#) due to plastic deformation, the higher the ductility and the shorter the length of the oil/gas pipeline failure is. In routine practice, [impact toughness](#) is commonly used as an integral [measure](#) of fracture resistance, to the first approximation [\[26\]](#), [\[27\]](#), [\[28\]](#).

Plastic deformation of grains has been investigated in [great details](#), c.f. [\[29\]](#), [\[30\]](#), [\[31\]](#). The influence of microscopic [deformation mechanisms](#) is commonly addressed through the use of the appropriate phenomenological relationships between strain/stress, grain size and [dislocation density](#). Nevertheless, [multi-scale](#) studies of the processes occurring under impact loading have not received sufficient coverage in the literature up to date. In addition, the issues in establishing the relationship between microstructure parameters and mechanical (macro) properties are still topical, and are of great scientific and practical interest [\[32\]](#), [\[33\]](#), [\[34\]](#).

There are also a number of additional factors that significantly affect the [fracture behaviour](#) and the toughness of pipe steel, which have to be accounted for. Specifically, modern [low-carbon steels](#) produced by thermomechanical processing of the original sheet are characterized by different sensitivity to the geometry of the

stress [concentrator](#) and temperature-strain [loading parameters](#) [35], [36], [37], [38], [39]. Another important problem is the characterization of [failure mechanisms](#) with different stress stiffness. The exceptional importance of this problem stems from the practical applications that are associated with the interpretation of elastoplastic characteristics of [structural material](#) resistance fracture where operational defects are identified. A major [breakthrough](#) in understanding the mechanism of [crack propagation](#) has been made in Ref. [40] where two new [important parameters](#) are introduced: the radius of the [core region](#) at the crack tip and the angle between the previous direction of crack growth and the direction of the [external load](#) applied. Numerous experimental data indicate that before the crack “rapid” unstable growth begins, the [micro-scale](#) fracture areas start forming at a finite distance from the crack tip [41]. In this context, the concept of [strain energy density](#) (SED) was evolved as a fundamental criterion of fracture. For [rapid crack propagation](#), reaching the critical value of the strain energy density multiplied by the radius of the core region is required. The term “*S-factor*” was coined by the author for this product. As mentioned above, the critical fracture stress is also dependent on the tensile [load angle](#) at the crack tip. The paper [42] also provided the mathematical calculations relating the materials [macroscopic](#) elastic constants, the [critical stress](#) and the direction of the [applied load](#). The model was then developed for triaxial [stress space](#). Describing the cracks in [cylindrical coordinates](#) enabled reducing the number of critical parameters to three ones depending only on one coordinate – direction of crack propagation.

Two mechanisms of [energy absorption](#) are common in the solids under load – plastic deformation and change of the volume. Therefore, it is logical to represent the *S-factor* as a sum of two corresponding terms. The continuum theory elaborated in Ref. [40] provides a rigorous analytical derivation of these terms. However, the computational methods suitable for describing structural materials based on this theory are still scarce. Therefore, in the present paper we develop a discrete-continual method of excitable cellular automata which explicitly takes into account the [energy term](#) responsible for the volume change, and the term responsible for micro-rotations in the material leading to its local deformation. We assume that the crack tip core region radius in structural materials is directly related to the [materials volume](#) involved into [rotational](#) deformation. The dependence of the rate of defects (e.g. dislocations) generation on the intensity of rotational deformation was introduced in the model. The absorption of [elastic energy](#) due to generation of lattice defects is accounted for in the model formulations. Another [important factor](#), which has to be considered in the development of the energy density theory, is temperature [43], [44] that significantly

affects the state of the loaded material, its elastic properties, plastic deformation and [fracture mechanisms](#).

Using [computer simulation](#), we endeavour to investigate the effect of [low temperature](#) on initiation of rotation [deformation modes](#) at the crack tip, and to clarify the significance of the notch shape and material structure. The macroscopic shape of the notch, with explicit consideration of the material [grain structure](#), was found to play a very marginal role in initiation of core region at the mesoscale level in the area of the [notch tip](#). The microstructure and the temperature are the most significant factors.

Thus, the objective of the present paper is to get a deeper insight into the role the energy factors in impact deformation and fracture with explicit accounting of the internal grain structure, temperature and geometry of the notch. Commercial plain [carbon pipe steel](#) 17Mn1Si, which has been widely accepted in industry, is used as a representative example. We employed the [theoretical method](#) of excitable cellular automata and performed laboratory impact [bending tests](#) followed by fractographic analysis. Experimental studies of the [dynamic deformation](#) and fracture were complemented by concurrent recording and time-frequency analyzing of [acoustic emission](#) signals [\[45\]](#), [\[46\]](#), [\[47\]](#), [\[48\]](#).

2. Excitable cellular automata method with account for deformation-induced defect structures

Using the method of excitable cellular automata [\[49\]](#) the effect of temperature on the stress-strain state evolution of the 17Mn1Si steel was studied. In doing so, the consideration was given to the existing [polycrystalline](#) structure of the material, the initiation of curvature at [grain boundaries](#) and dissipation of [elastic energy](#) as a result of micro-rotation.

In the present version of the excitable cellular automata method, the distinction is made between a network of 2D interface boundaries and the 3D-subsystem composed of crystalline grains. The interaction between these two is implemented by simulation of initiation of new defect (dislocation) structures at grain boundaries and their propagation into the [grain interior](#). Accordingly, the method was improved by adding specific expressions for computation of the [defect density](#) and the mobility of the material as a function of this density. Description of a new modification of the algorithm is given below.

The simulated sample is presented in the form of a cellular automaton representing the network of elements. This network is divided into clusters where each one is

responsible for a [single grain](#) with its own crystalline lattice orientation vector $\theta \rightarrow$ with Euler angles ψ, φ, η as its coordinates: $\theta \rightarrow (\psi, \varphi, \eta)$.

The [model input](#) parameters include the initial values of the hydrostatic pressure p , density ρ and temperature T of each element, i.e. a set $\{p_{i0}, \rho_{i0}, T_{i0}; 0 \leq i < l\}$, where l is the total number of elements, the superscript index corresponds to the time step number n . The initial [mechanical energy](#) of the element with index i (E_{i0}) is calculated as follows:

$$(1) E_{i0} = p_{i0} \cdot \Lambda_c,$$

where Λ_c is the [element volume](#).

The value of the mechanical energy of the element with index i in the n -th time step (E_{in}) depends on its [energy value](#) in the $(n-1)$ -th time step (E_{in-1}) and the total flow of energy from its [nearest neighbours](#), i.e. the elements located in its first coordination sphere (ΔE_{in}), and is calculated as follows:

$$(2) E_{in} = E_{in-1} + \Delta E_{in}, \Delta E_{in} = \sum_{k=0}^{K-1} \Delta E_{ikn}.$$

Here ΔE_{ikn} is the change in the mechanical energy of the i -th element as a result of the interaction with the k -th element in the first coordination sphere ($0 \leq k < K$, K is the number of elements in the first coordination sphere) in the n -th time step. ΔE_{ikn} is calculated as follows.

1.

The stress at the ζ_{ikn-1} boundary of the i -th element and its k -th neighbour in the $(n-1)$ -th time step is found as the difference of the hydrostatic [pressures applied](#) from each of the pair of elements is calculated:

$$(3) \zeta_{ikn-1} = p_{kn-1} - p_{in-1}.$$

2.

Using the Turnbull formula, the [boundary velocity](#) v_{ikn} under given stress ζ_{ikn-1} is calculated as:

$$(4) v_{ikn} = -\kappa_{ik} \cdot \zeta_{ikn-1}.$$

where κ_{ik} is the boundary mobility between i -th element and its k -th neighbour.

In the framework of the [simulation method](#) the effects of plasticity are taken into account through variation of material mobility resulted from nucleation of new [defect structures](#).

The changing of [dislocation density](#) is calculated being based on [rotational deformation](#) components [49]. As it will be shown below, the dislocation density is then used for calculating activation energy value.

Let N_{in} and N_{kn} be the numbers of atoms contained in the i -th element and its k -th neighbour, respectively, and

$$(5) N_{jn-1} = \rho_{jn-1} \Lambda_c (\mu \text{mol})_j N_A,$$

where ρ_{jn} is the material's density of the j -th element in the n -th time step, $(\mu \text{mol})_j$ is [molar mass](#) of the material contained in the j -th element, Λ_c is the element volume, N_A is the Avogadro's number. For the further model construction we should take into account l_{ik} - the activation energy of the boundary between the i -th element and its k -th neighbour.

In the current research all grain boundaries are considered to be of low-angle origin (this is a serious limitation of the model which has yet to be elaborated in the future research). Therefore the Shockley-Read approximation [\[49\]](#), [\[50\]](#), [\[51\]](#) applies for the grain boundary energy:

$$(6) l_{ik} = \gamma_{HAGB} \Delta(\theta \rightarrow i, \theta \rightarrow k) \theta_{HAGB} (1 - \ln \Delta(\theta \rightarrow i, \theta \rightarrow k) \theta_{HAGB}), \Delta(\theta \rightarrow i, \theta \rightarrow k) > 0, \Delta(\theta \rightarrow i, \theta \rightarrow k) = 0.$$

Here γ_{HAGB} is a maximum boundary energy corresponding to the maximum angle of the crystalline lattice misorientation θ_{HAGB} , $\Delta(\theta \rightarrow i, \theta \rightarrow k)$ denotes a function that determines the misorientation angle between the grains lattices containing the i -th element and its k -th neighbour, $0 \leq \Delta(\theta \rightarrow i, \theta \rightarrow k) \leq \theta_{HAGB}$.

For low-angle grain boundaries, the misorientation function $\Delta(\theta \rightarrow i, \theta \rightarrow k)$ is set at 0 for any coinciding pairs of [grain orientation](#) vectors of the i -th $\theta \rightarrow i(\psi_i, \phi_i, \eta_i)$ and the k -th $\theta \rightarrow k(\psi_k, \phi_k, \eta_k)$ element. This function is determined as follows:

$$(7) \Delta(\theta \rightarrow i, \theta \rightarrow k) = (\psi_i - \psi_k)^2 + (\phi_i - \phi_k)^2 + (\eta_i - \eta_k)^2,$$

and the values of the Euler angles for each grain (ψ, ϕ, η) belong to the interval $[0; \theta_{HAGB}]$.

There is a possibility to explicitly consider the formation of new dislocations in the expression for the material mobility at the boundary between [active elements](#). The value of the boundary mobility between the i -th element and its k -th neighbour is computed from the equation that accounts for the particular type of material contained in each of the subject elements. The activation energy of the boundary between the microstructural elements and the energy of defects generated during [plastic deformation](#) is given as:

$$(8) \lambda_{ikn-1} = (\lambda_0)_{ik} \cdot e^{-l_{ik} + Q_{in-1} - Q_{kn-1}} k_B T_{ikn-1},$$

where $(\lambda_0)_{ik}$ is an empiric parameter, T_{ikn-1} is the temperature at the boundary of the i -th element and its k -th neighbour, l_{ik} is the activation energy of the boundary between

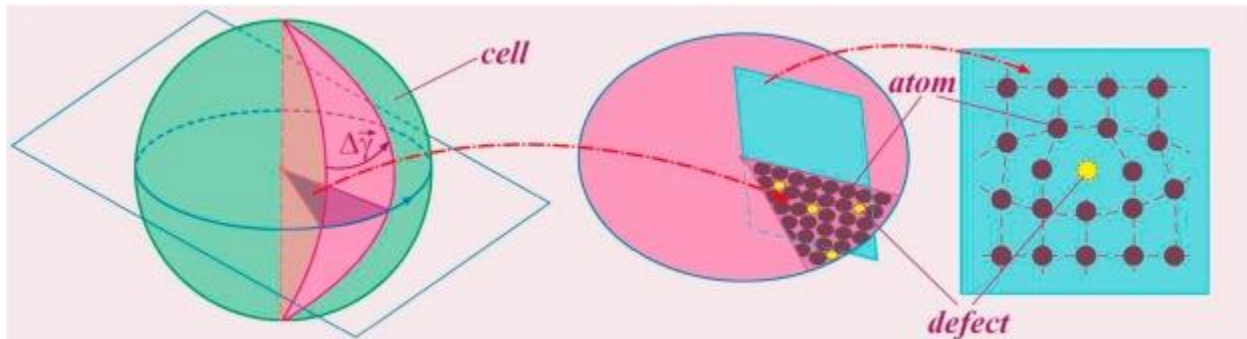
the i -th element and its k -th neighbour, Eq. (6), Q_{in-1} , Q_{kn-1} are the values of the cumulative energy of crystal defects contained in the i -th element and its k -th neighbour: (9) $Q_{in-1}=\eta_{in-1}kBT_{in-1}\ln N_{in-1}\eta_{in-1}$, $Q_{kn-1}=\eta_{kn-1}kBT_{kn-1}\ln N_{kn-1}\eta_{kn-1}$,

where η_{in-1} , η_{kn-1} are the numbers of defects contained in the i -th element and its k -th neighbour, respectively and N_{in-1} and N_{kn-1} are the numbers of atoms contained in the i -th element and its k -th neighbour, respectively. Substituting Eq. (9) into Eq. (8), we obtain:

$$(10)\lambda_{ikn-1}=(\lambda_0)_{ik}\cdot e^{-\frac{Q_{in-1}+Q_{kn-1}}{kBT_{in-1}}}\cdot N_{in-1}^{\eta_{in-1}}\cdot T_{in-1}^{\eta_{in-1}}\cdot N_{kn-1}^{\eta_{kn-1}}\cdot T_{kn-1}^{\eta_{kn-1}}$$

It is worth highlighting that the energy of lattice defects, e.g. dislocations, does not significantly affect the grain boundary mobility if the defects are located far away from the boundary. The parameter Q in Eq. (9) and hereinafter is entered cumulatively, which is one of the limitations of the proposed model.

The change in the number of new dislocations generated in the element during torsion of the material is computed [52]. An intersection of the dislocation with the atomic plane (see Fig. 1) is treated as a new “defect state” of crystal structure in terms of cellular automata.



1. [Download high-res image \(92KB\)](#)
2. [Download full-size image](#)

Fig. 1. The diagram of computation of the change in the number of defect states in the element during torsion of the material.

As shown in Fig. 1, a locally curved region of the crystal lattice forms in the region of dislocation core that generates the driving force for the motion of defects even with no external load. Modelling the motion of such defects in the material local volume is realized on the basis of the method of Bistable Cellular Automata (BCA). Each bistable automata element has two probable states – “atom” and “defect”. The rules of element switching depend on the states of neighbouring elements and on the values of the energy parameters describing its state.

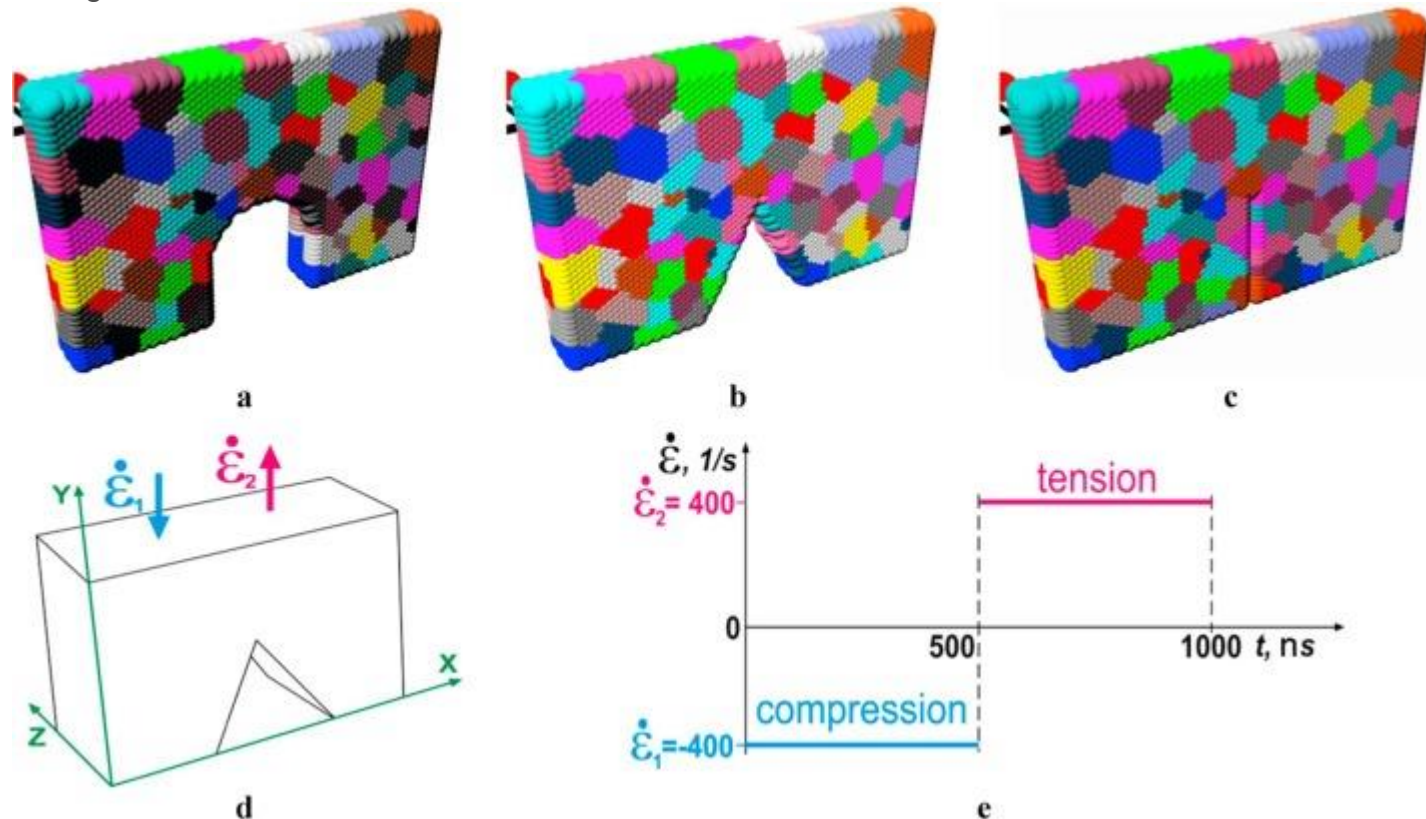
Each element of the Stochastic Excitable Cellular Automata - SECA network (termed excitable element) is represented as bistable cellular automata, i.e. a network of bistable elements. As soon as the SECA computation method time step is over, the time cycle of BCA method starts. Inside the BCA method for each bistable element it is defined whether it will switch to a new state, or will remain as is. In the first step of the time cycle in accordance with the current value of the defect density in the excitable element η_{in} the states of the bistable elements contained therein are defined. If the value η_{in} increased compared to the previous step, i.e. $\Delta\eta_{in}>0$, the elements in the state of “defect” remain unchanged, while the elements in the state of “atom” stochastically switch to another state thus attaining the current value of the defect density η_{in} . At each next time step of the BCA, the elements are re-distributed in the state of “defects” across the network so that the elements in the state of “defect” are gradually attracted to each other in the attempt to form a defect of greater [size \(crack or pore\)](#).

The proposed approach therefore translates into practice the physical mesomechanics concept highlighting the fundamental role of the crystalline lattice curvature as the root cause of crack nucleation. In this regard, a special attention was paid to the calculation and analysis of such [internal dynamic](#) parameters as the [angular velocity](#) of the material torsion, the total cumulative [angle of rotation](#) of the medium, and the amount of [dissipated energy](#) in the course of defect structure initiation.

3. Numerical simulation of high-speed loading at different temperatures of steel specimens with variously shaped notches

For the numerical analysis of the [deformation](#) behaviour of specimens (meso-volume) of the [model material](#) identical in structure and properties at different [testing temperatures](#) (ranging from $T = 213$ K to $T = 293$ K with the increment $\Delta T = 20$ K) using SECA method, a series of [numerical simulations](#) (NS) were undertaken for [impact loading](#) of specimens with U-, V- and I-shaped notches. The [energy dissipation](#) is explicitly taken into account in those simulations in local rotations of the material. At the same time, the [mechanical energy](#) change of each cellular automaton element determines the increase of the material torsion energy in the element proportionally to the coefficient of dissipation which is an increasing function of the material temperature. Each specimen of $150 \times 100 \times 10 \mu\text{m}^3$ dimensions is presented as a cellular automaton with the FCC crystalline lattice for each element of $2.6 \mu\text{m}$ size. The grain size is taken equal to $13 \mu\text{m}$ ([Fig. 2a–c](#)). The time step is set at 10 ns and the NS total time is 1 μs . The initial values of stress and strain are equal to zero. For all specimens, [boundary conditions](#) are specified that exclude the influence thereon of the [external environment](#).

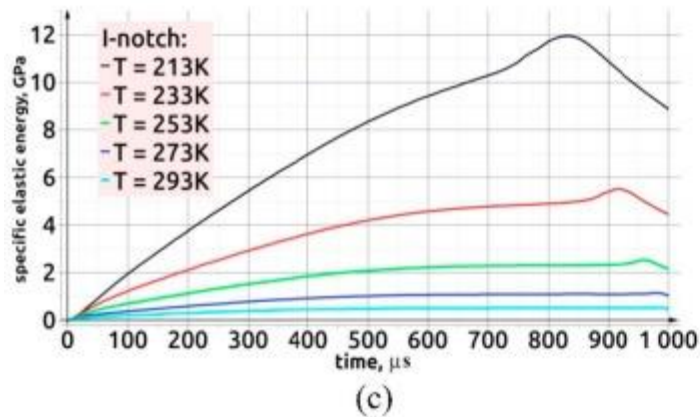
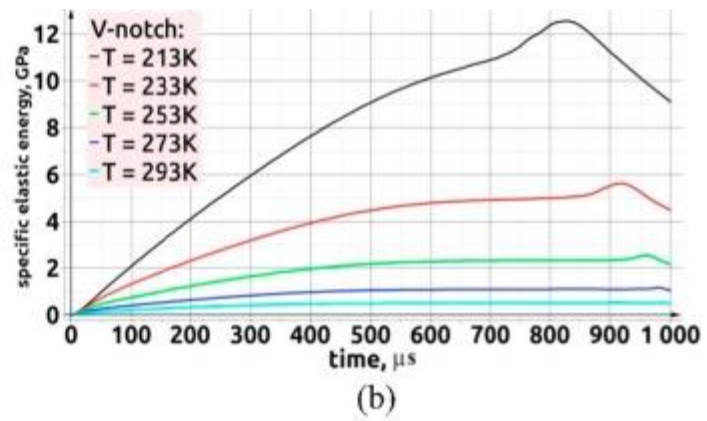
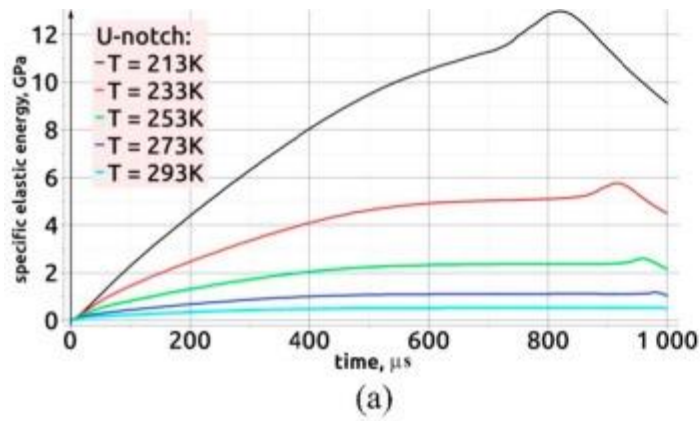
First the top face is subjected to [compressive loading](#) with a [strain rate of](#) 400 s^{-1} during $0.5 \mu\text{s}$. Then, for the remaining $0.5 \mu\text{s}$, the [loading direction](#) changes to tension on the top face side with the same [strain rate](#) ([Fig. 2d](#) and [e](#)). No [energy exchange](#) is assumed through the other boundaries.



1. [Download high-res image \(260KB\)](#)
2. [Download full-size image](#)

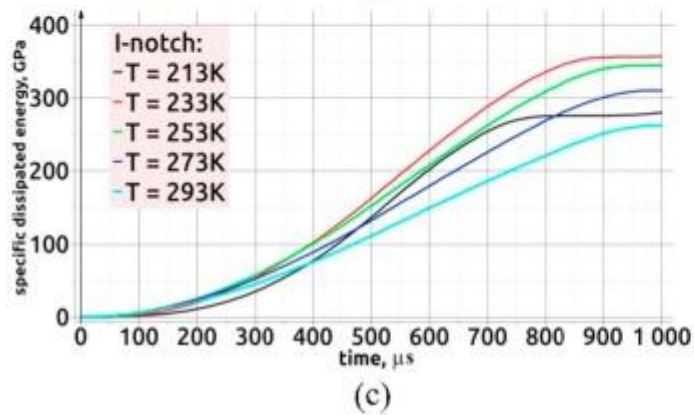
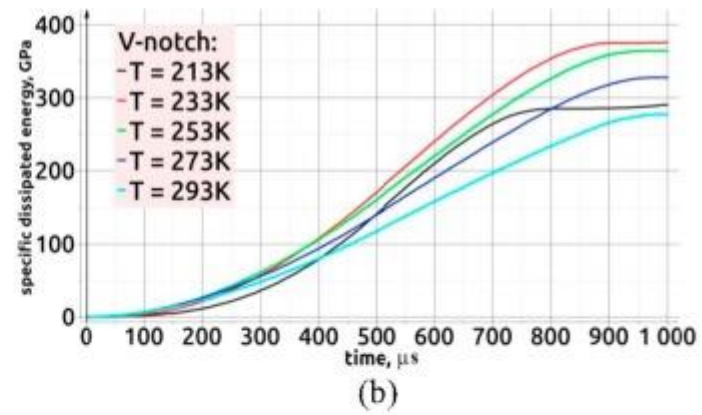
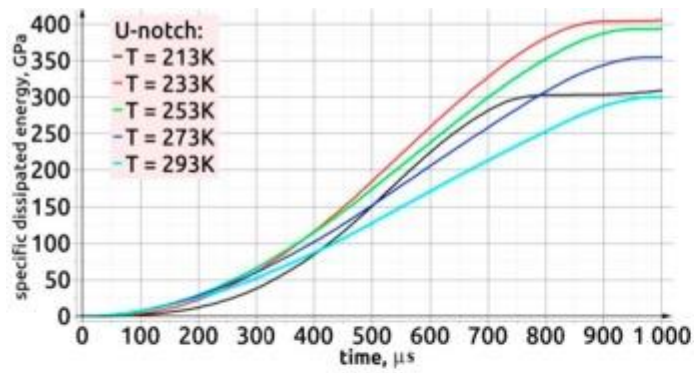
Fig. 2. Diagrams of specimens with U- (a), V- (b) and I-shaped (c) notches, [deformation](#) diagram (d), and time dependence plot for the load (e).

[Fig. 3](#), [Fig. 4](#), [Fig. 5](#), [Fig. 6](#), [Fig. 7](#), [Fig. 8](#) show the time-dependence plots for specific (over volume) values of the [elastic energy](#) dissipated as a result of local rotations, relative [dissipated energy](#) (ratio of the dissipated energy to the total mechanical energy), average modulus of local [angular velocity](#) of material in the element, and average modulus of [material local](#) torsion angle, as well as the graph, showing the dependence of the specific elastic energy on the mean [normal strain](#) (i.e. the strain integrated over the entire volume related to such volume). These plots were produced for each of the specified temperature values and for the entire volume of specimens with U-, V- and I-shaped notches with the exception of $2.6 \mu\text{m}$ thick [boundary layers](#).



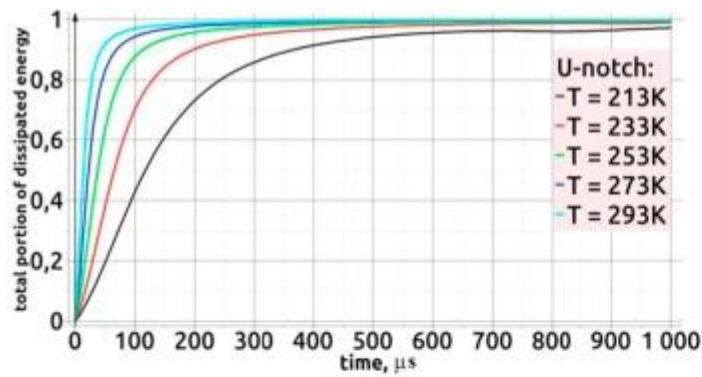
1. [Download high-res image \(193KB\)](#)
2. [Download full-size image](#)

Fig. 3. Specific [elastic energy](#) vs. time plots for the specimens with U-, V- and I-shaped notches at various temperatures (black line – 213 K, red – 233 K, green – 253 K, dark blue – 273 K, [light blue](#) – 293 K). (For interpretation of the references to colour in this figure legend, the reader is referred to the web version of this article.)

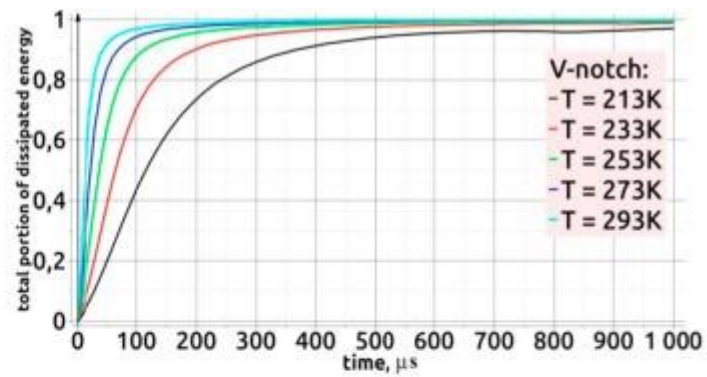


1. [Download high-res image \(202KB\)](#)
2. [Download full-size image](#)

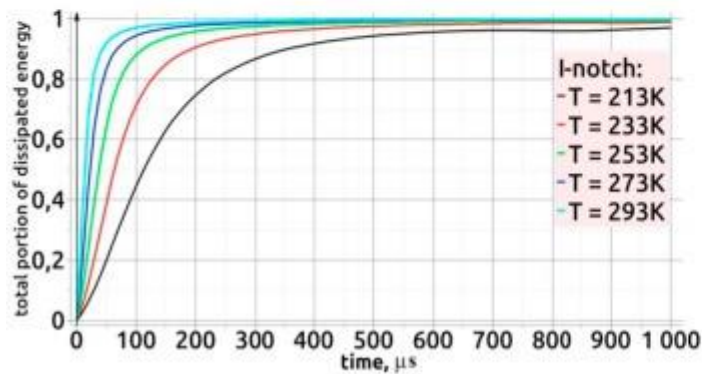
Fig. 4. Specific [dissipated energy](#) vs. time plots for the specimens with U-, V- and I-shaped notches at various temperatures (black line – 213 K, red – 233 K, green – 253 K, dark blue – 273 K, [light blue](#) – 293 K). (For interpretation of the references to colour in this figure legend, the reader is referred to the web version of this article.)



(a)



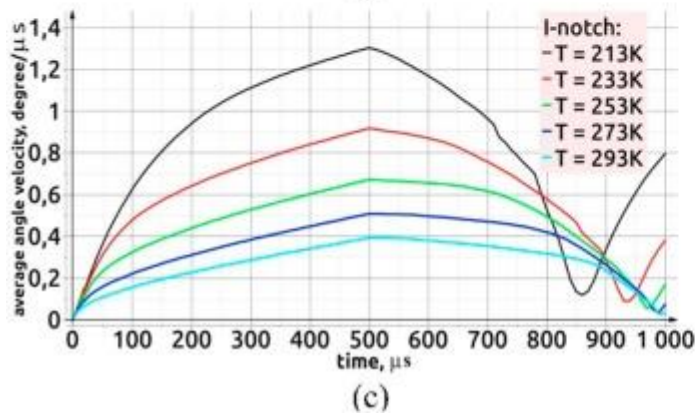
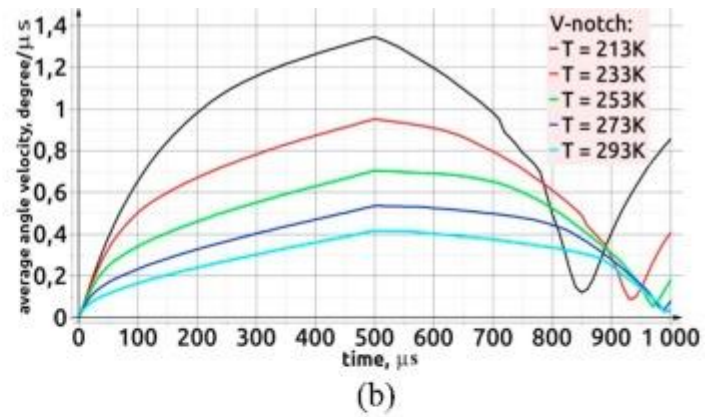
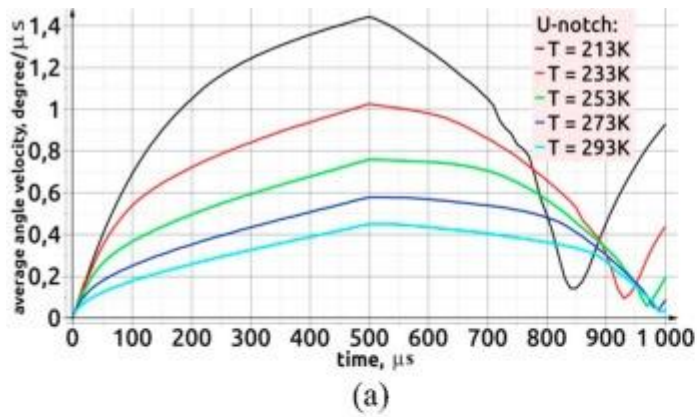
(b)



(c)

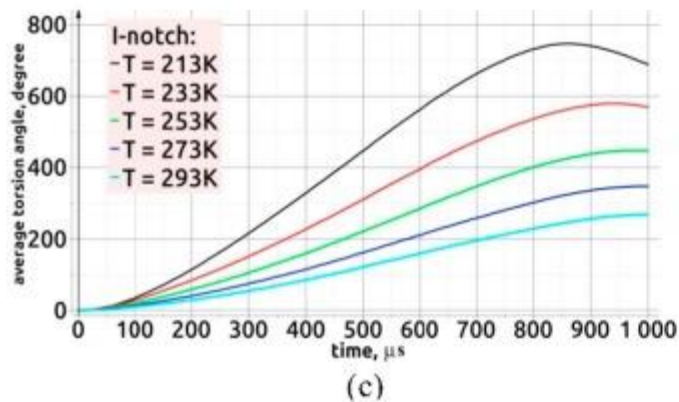
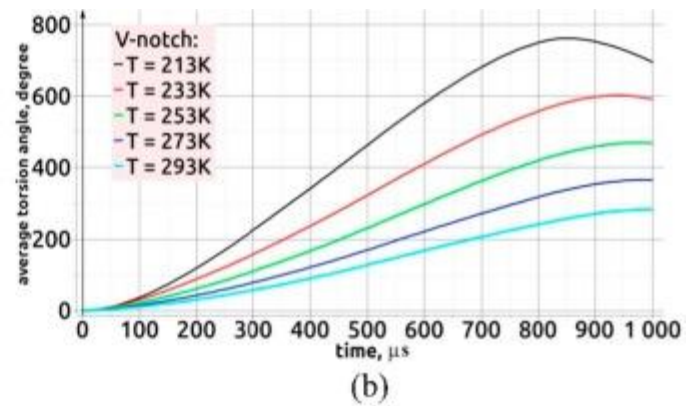
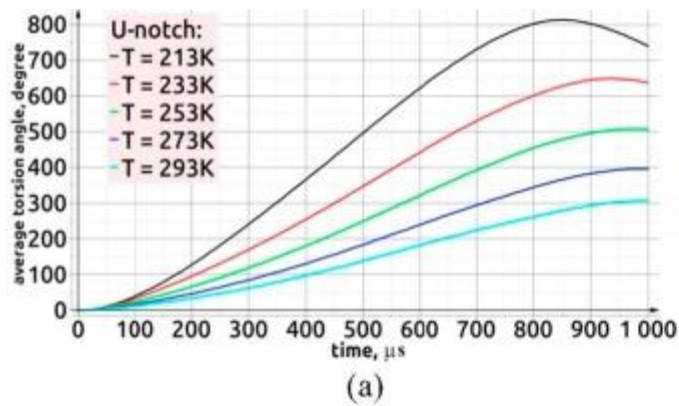
1. [Download high-res image \(194KB\)](#)
2. [Download full-size image](#)

Fig. 5. Relative [dissipated energy](#) vs. time plots for the specimens with U-, V- and I-shaped notches tested at different temperatures (black line – 213 K, red – 233 K, green – 253 K, dark blue – 273 K, [light blue](#) – 293 K). (For interpretation of the references to colour in this figure legend, the reader is referred to the web version of this article.)



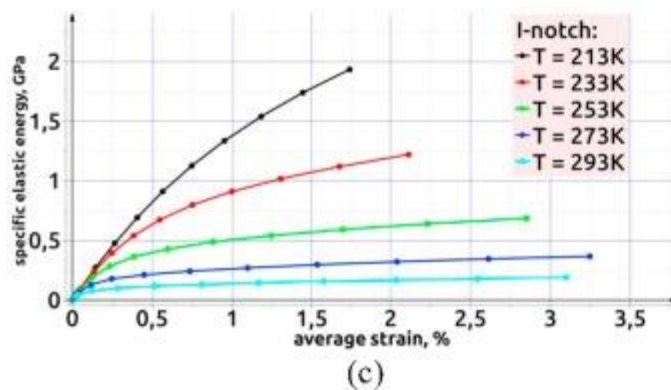
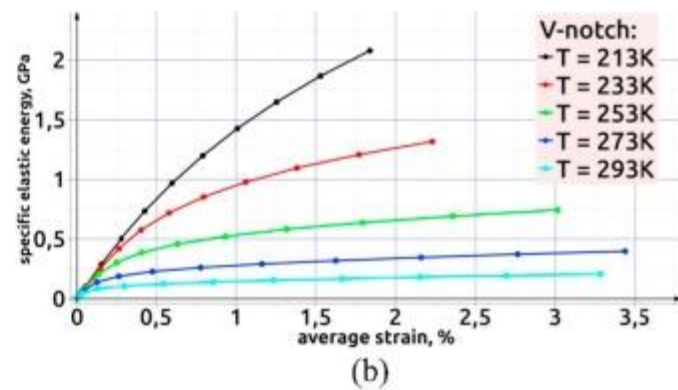
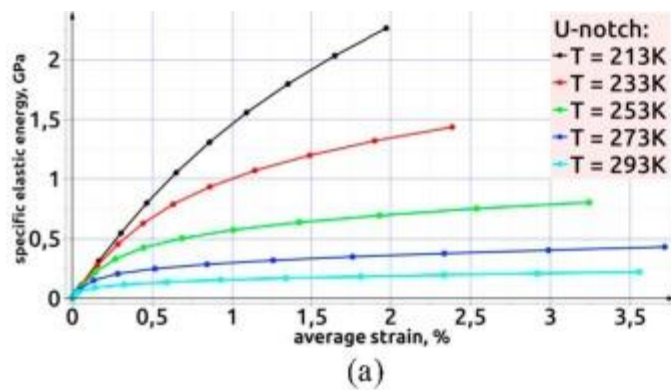
1. [Download high-res image \(238KB\)](#)
2. [Download full-size image](#)

Fig. 6. The plots representing the average absolute value of the material's local rotation angular velocity vs. time for the specimens with U-, V- and I-shaped notches tested at different temperatures (black line – 213 K, red – 233 K, green – 253 K, dark blue – 273 K, light blue – 293 K). (For interpretation of the references to colour in this figure legend, the reader is referred to the web version of this article.)



1. [Download high-res image \(199KB\)](#)
2. [Download full-size image](#)

Fig. 7. The plots representing the behaviour of the average [absolute value](#) of the material's local torsion angle as a function of. time for the specimens with U-, V- and I-shaped notches tested at different temperatures (black line – 213 K, red – 233 K, green – 253 K, dark blue – 273 K, [light blue](#) – 293 K). (For interpretation of the references to colour in this figure legend, the reader is referred to the web version of this article.)



1. [Download high-res image \(183KB\)](#)
2. [Download full-size image](#)

Fig. 8. Specific [elastic energy](#) as a function of mean strain for the specimens with U-, V- and I-shaped notches tested at different temperatures (black line – 213 K, red – 233 K, green – 253 K, dark blue – 273 K, [light blue](#) – 293 K). (For interpretation of the references to colour in this figure legend, the reader is referred to the web version of this article.)

As seen in [Fig. 3](#), the response of specimens to the alternating load appears similar, but differs in the level. The lower the test temperature, the greater the specific elastic energy is; furthermore, the energy increase is non-linear with the temperature reduction. It should be noted that the level of elastic energy transferred through a meso-volume keeps increasing even after the beginning of the tension half-cycle. This means that raising the test temperature up to $T = 293$ K activates specific mechanisms of elastic energy relaxation due to formation of defect flows along the [grain boundaries](#) causing such appreciable reduction in the specimen [elastic response](#) at room temperature. As described earlier, the boundaries between the [structural elements](#) constitute a 2D-subsystem that serves a source of virtually all stress/strain-induced [deformation processes](#). This circumstance is especially relevant under [high-speed](#) loading, where the processes of dissipation of the elastic energy “injected” into the specimen can

significantly increase the energy of the impact fracture. This is supported by the specific dissipated energy (SDE) vs. loading time plots, [Fig. 4](#), which clearly shows that with [increasing temperature](#) the SDE maximum value reduces due to the intensification of defect formation at the grain boundaries. This suggests that the development of [dissipative processes](#) allows the absorption of energy induced into the specimen, thereby providing resistance to future fracture.

A series of simulations with the specimens at the lowest temperature $T = 213$ K are of particular interest. It is obvious that at a given temperature at the stage $t \sim 750 \mu\text{s}$ the dissipated energy curves for all three types of notches tend to saturation, and the beginning of such a saturation stage coincides with the onset of the above mentioned abnormal elastic energy rise shown in [Fig. 3](#).

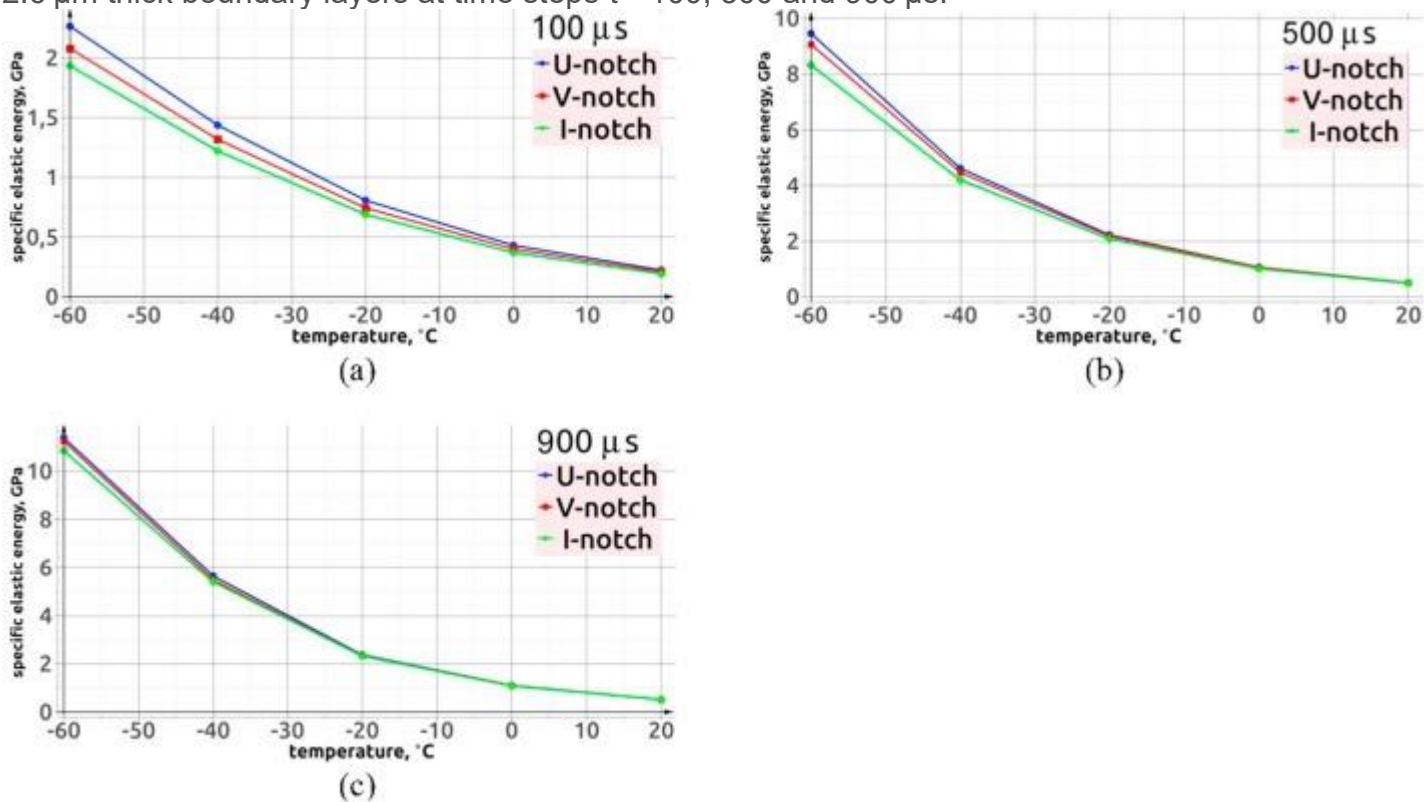
To confirm the assumption about the intensification of the process of defect formation with increasing temperature, the time dependence of the relative dissipated torsion energy was plotted in [Fig. 5](#). The relative dissipated elastic torsion energy denotes the fraction of the elastic torsion energy spent on the formation of new defects. As can be seen from the graphs in [Fig. 5](#), the loading curve at room temperature is the first to arrive at saturation, displaying that beginning from $t \sim 200 \mu\text{s}$ virtually all energy injected into the specimen is consumed by defect formation.

In this respect, it is very important to pay attention to the essentially inertial character of the processes occurring in the [polycrystal](#). [Fig. 3](#) shows that the drops in the average level of the elastic energy occur much later than the beginning of the unloading half-cycle. In addition, all curves exhibit visible stages of the abnormal gain of elastic energy, which begin the earlier, the lower the test temperature is. The duration of the stages corresponding to the abnormal elastic energy rise is also related to the test temperature in the reciprocal way: the lower the temperature, the greater the duration of the stage of the elastic energy abnormal gain is. This anomaly can be explained by the difference in the elastic energy flow velocities in grain bodies and rotating-wave [energy fluxes](#) along the grain boundaries. Such rotating-wave fluxes were described by some of the authors in [\[2\]](#). At the unloading stage, the two opposite flows inside grain bodies collide with the fluxes along grain boundaries. This is corroborated by the shape of time dependences of angular velocities and cumulative angles of torsion shown in [Figs. 6](#) and [7](#), respectively.

Active involvement of dissipative processes at higher test temperature is clearly confirmed by the specific elastic energy vs. mean strain dependence shown in [Fig. 8](#). Despite the quantitative differences in the magnitude of the total strain and [maximum stress](#) (within 30%), all three notch specimens behave qualitatively similarly. This is

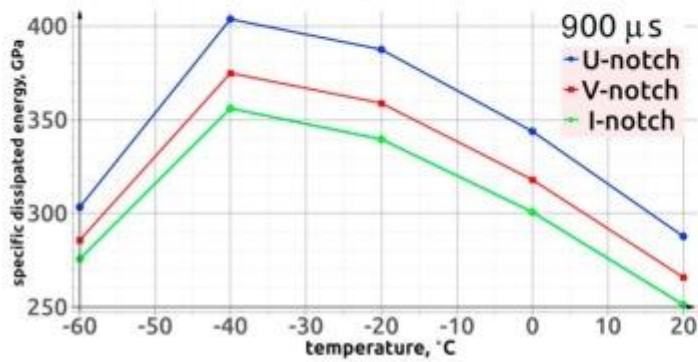
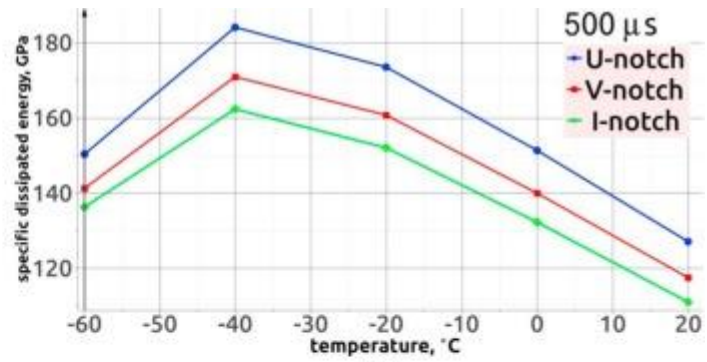
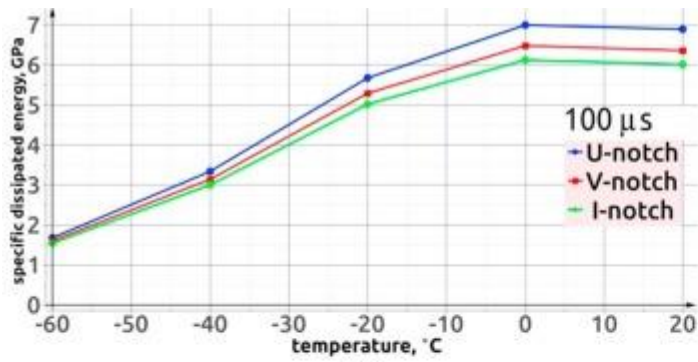
indicative of the dominant role of the temperature factor in the [dynamic deformation](#) response of [polycrystals](#).

[Fig. 9](#), [Fig. 10](#), [Fig. 11](#), [Fig. 12](#), [Fig. 13](#) display the [temperature dependences](#) of the following quantities: the elastic energy density, energy dissipated due to local rotations, relative dissipated energy (ratio of the dissipated energy to the total mechanical energy), average modulus of local angular velocity of material in the element, and average modulus of material local torsion angle. These dependences are defined for the entire volume of specimens with U-, V- and I-shaped notches with the exception of 2.6 μm thick boundary layers at time steps $t = 100, 500$ and $900 \mu\text{s}$.



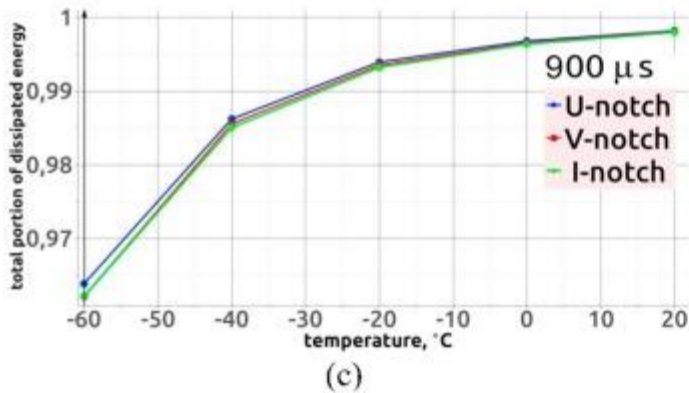
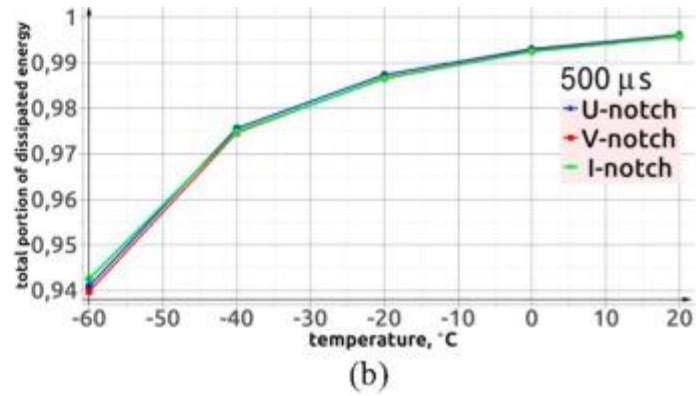
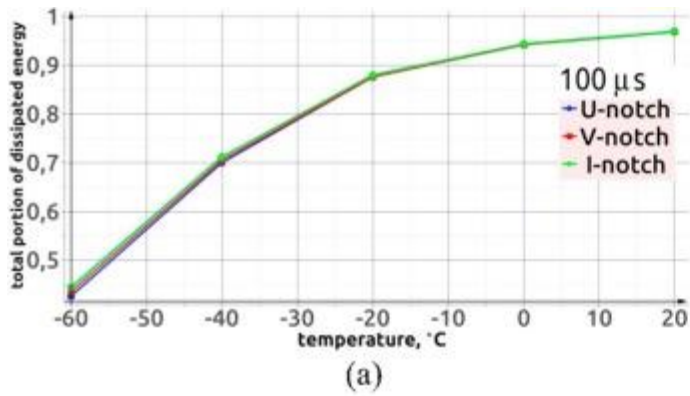
1. [Download high-res image \(153KB\)](#)
2. [Download full-size image](#)

Fig. 9. Specific [elastic energy](#) as a function of temperature for the samples with U- (blue plot), V- (red), and I-shaped (green) notches at time points $t = 100$ (a), 500 (b) and 900 (c) μs . (For interpretation of the references to colour in this figure legend, the reader is referred to the web version of this article.)



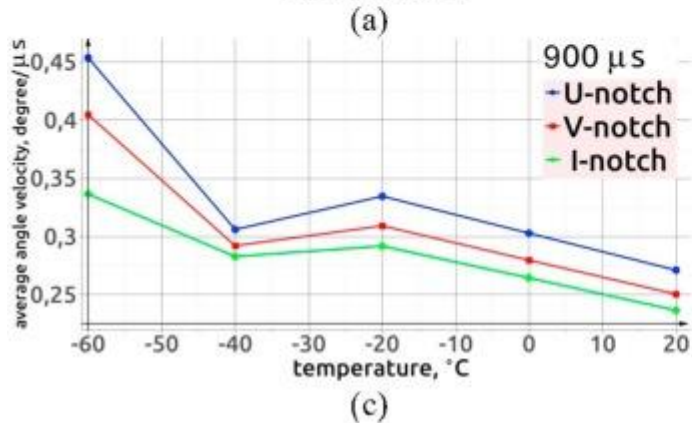
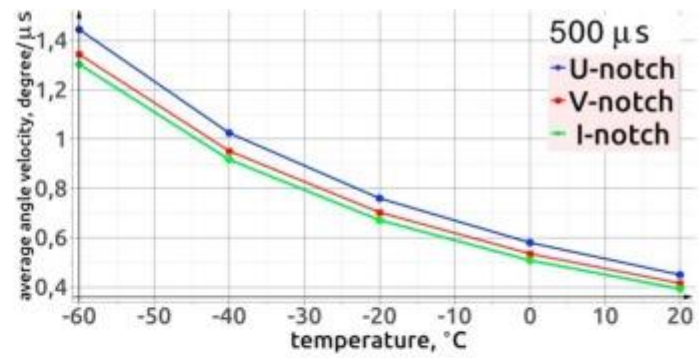
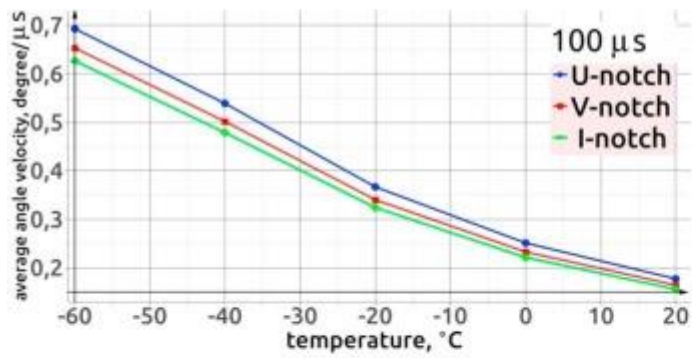
1. [Download high-res image \(185KB\)](#)
2. [Download full-size image](#)

Fig. 10. Specific dissipated energy as a function of test temperature for the samples with U- (blue line), V- (red), and I-shaped (green) notches at time points $t = 100$ (a), 500 (b) and 900 (c) μs . (For interpretation of the references to colour in this figure legend, the reader is referred to the web version of this article.)



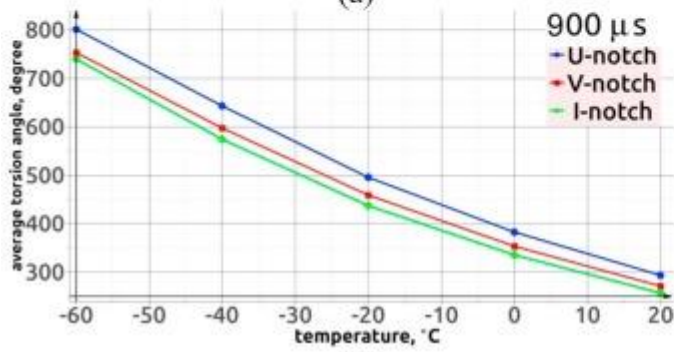
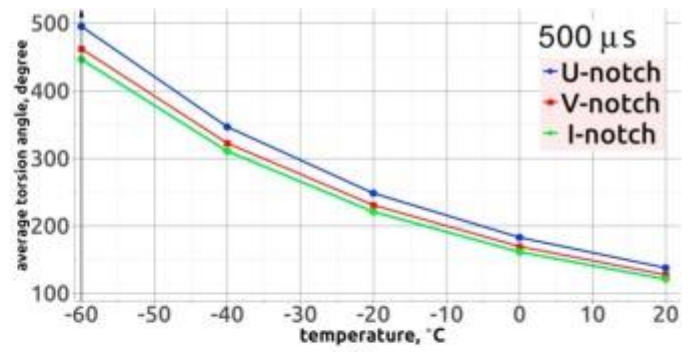
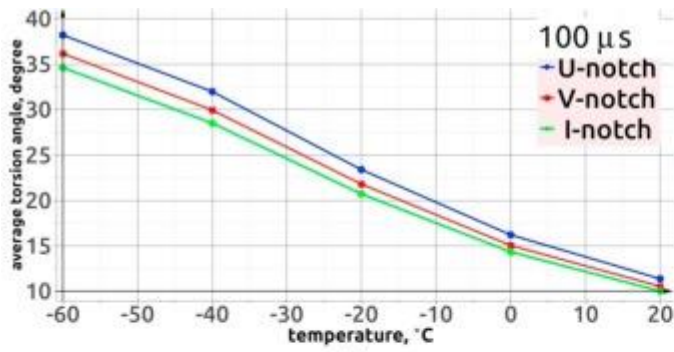
1. [Download high-res image \(160KB\)](#)
2. [Download full-size image](#)

Fig. 11. Relative [dissipated energy](#) as a function of temperature for the dynamically loaded samples with U- (blue line), V- (red), and I-shaped (green) notches at time points $t = 100$ (a), 500 (b) and 900 (c) μ s. (For interpretation of the references to colour in this figure legend, the reader is referred to the web version of this article.)



1. [Download high-res image \(183KB\)](#)
2. [Download full-size image](#)

Fig. 12. Dependence of the average [absolute value](#) of the [angular velocity](#) of local rotations on the test temperature for the samples with U- (blue line), V- (red), and I-shaped (green) notches at time points $t = 100$ (a), 500 (b) and 900 (c) μs . (For interpretation of the references to colour in this figure legend, the reader is referred to the web version of this article.)



1. [Download high-res image \(170KB\)](#)
2. [Download full-size image](#)

Fig. 13. Average absolute value of material local rotation angle as a function of temperature for the samples with U- (blue plot), V- (red), and I-shaped (green) notches at time points $t = 100$ (a), 500 (b) and 900 (c) μs . (For interpretation of the references to colour in this figure legend, the reader is referred to the web version of this article.)

The specific elastic energy versus temperature plots obtained for the samples with U-, V- and I-shaped notches at different loading stages show that the difference between the specimens with different notches is clearly manifested only early loading stages. The lower the test temperature, the greater the difference in the average elastic energy values is. This situation is clarified by the specific dissipated energy as a function of temperature represented in [Fig. 10](#). As can be seen, with increasing testing temperature the difference in the values of the dissipated energy increases too, i.e. the specimen at a higher temperature “adapts” itself more actively to the changing elastic energy, providing an effective relaxation of stress concentrators through the ongoing chain of processes initiating micro-rotations and new defects structures at the grain boundaries. The qualitative changes of the curves shown in [Fig. 10](#) should also be discussed. It is shown that before the loading stage ends at $t = 500 \mu\text{s}$, the dissipated energy reaches its maximum at $T = 233 \text{ K}$, decreasing thereafter as temperature rises. This prompts us to conclude that on the mesoscopic scale level in the area adjacent to

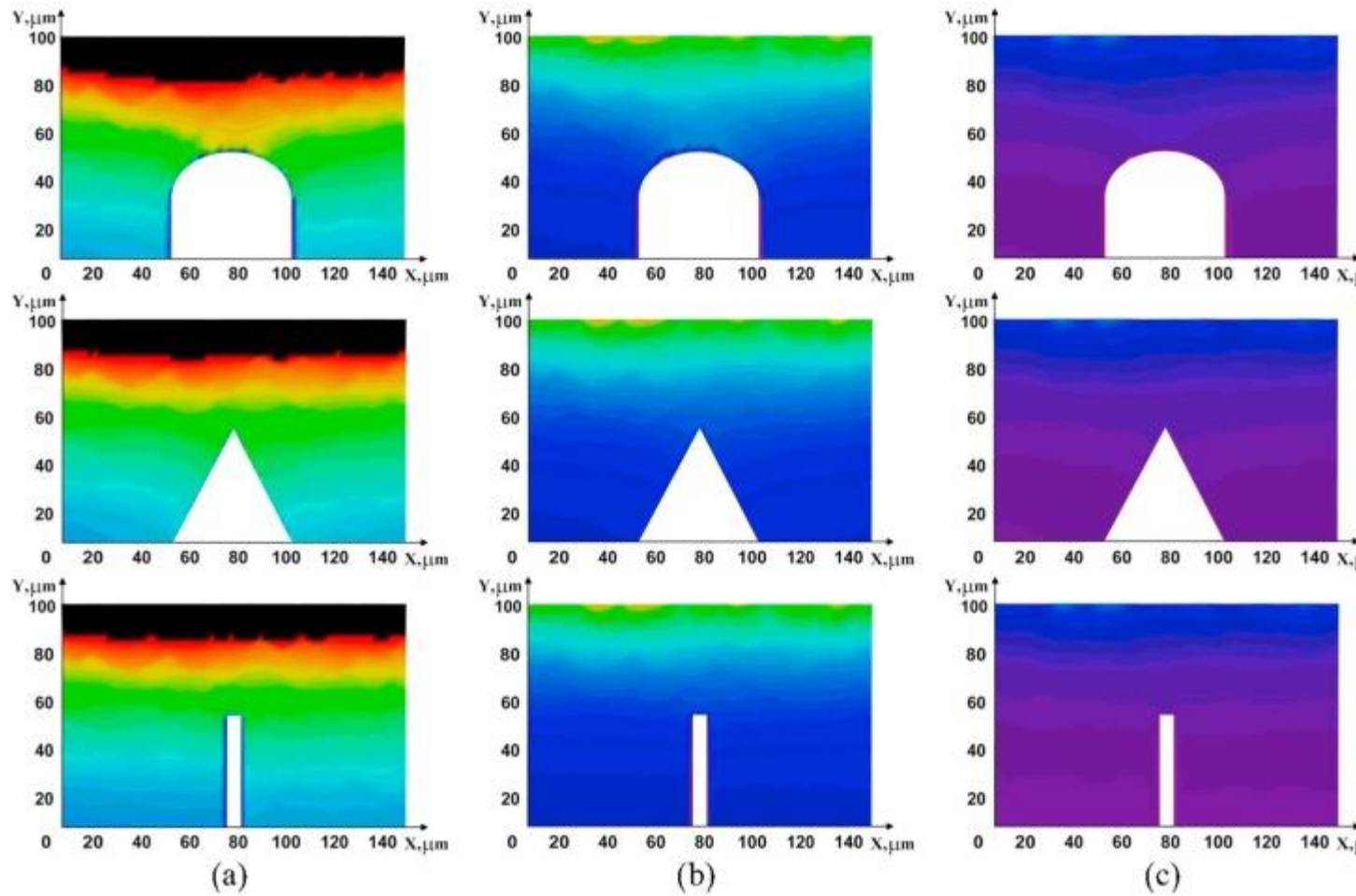
stress [concentrator](#), the durations of the elastic energy storage processes and its relaxation are dependent not only on the velocity of elastic energy flow and material properties, but also on the testing temperature. The above described process of specimen response “adaptation” to the changing [external stress](#) by efficient generation of defect structures is exemplified in [Fig. 11](#). We can see that the fraction of the dissipated energy monotonically increases with temperature for all specimens at both loading stages.

The results of comparison of temperature dependences of the average values of angular velocity against the cumulative [rotation angle](#) at the unloading stage shown in [Figs. 12c](#) and [13c](#), respectively, are particularly noteworthy. The local angular velocity reflects an essentially elastic component in the [material behaviour](#). The cumulative rotation angle, on the other hand, characterizes the cumulative effect of all [rotational](#) modes of deformation including the processes of accommodation and dissipation. It is shown that in spite of the non-linear dependence for the angular velocity, [Fig. 12c](#), the curves for the [absolute value](#) of the material local rotation angle decrease monotonically. This once again corroborates the thesis on the accommodative nature of the two synergistically related processes – the initiation of elastic micro-rotations and their compensatory generation of defects from grain boundaries. This implies that the difference in rates of defect production and accumulation of elastic torsion energy shall be deemed the criterion of [crack extension](#).

It is well known that the curl of all continuous displacements in the media must be zero at equilibrium. In the actual structurally heterogeneous solids, this condition does not hold at each instant of time. It is however fulfilled on average over a certain time interval. Therefore, the curl of the material rotation angle increment in the selected meso-volume should be deemed a crack extension criterion.

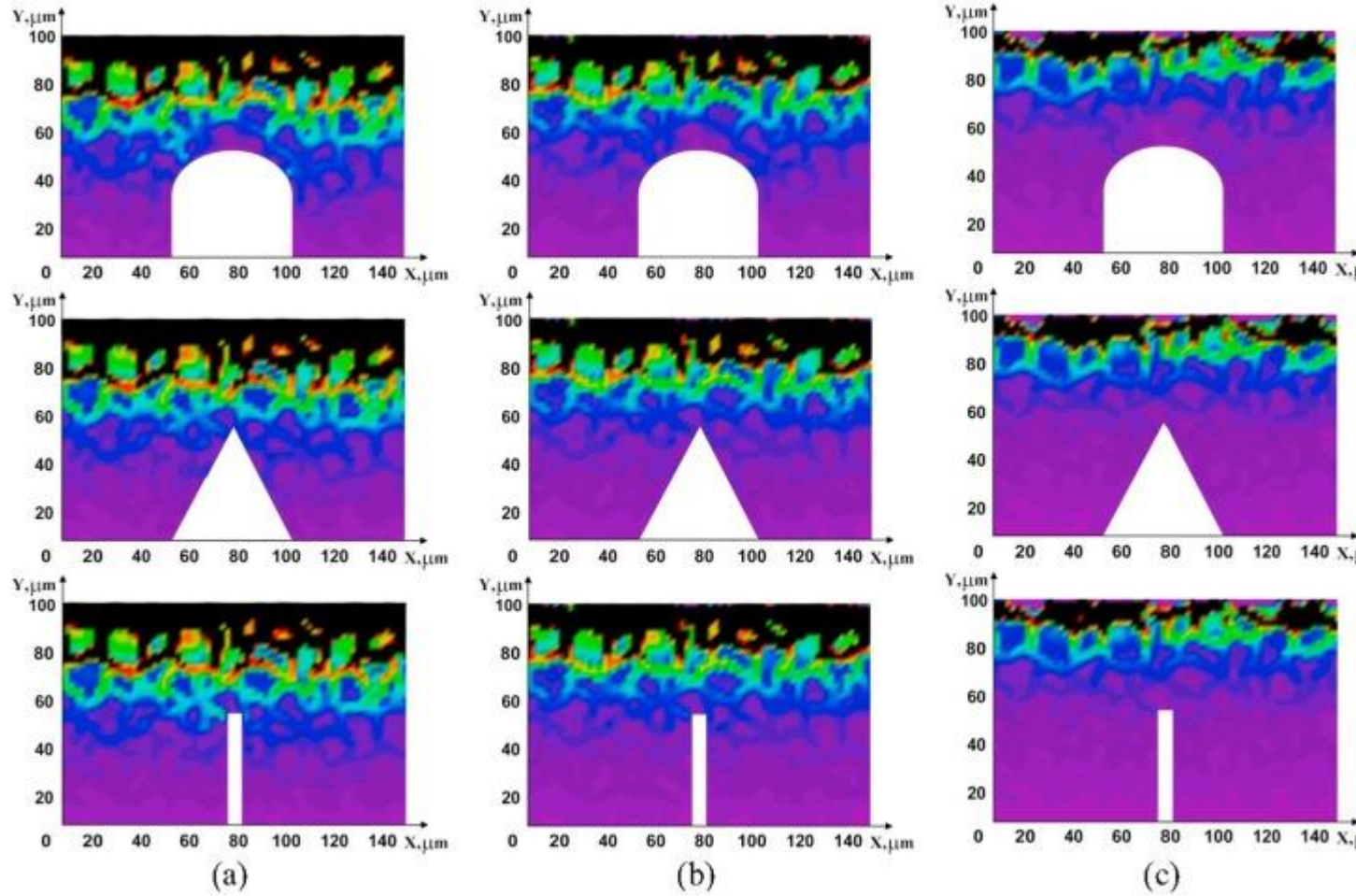
[Fig. 14](#), [Fig. 15](#), [Fig. 16](#), [Fig. 17](#) show the distribution patterns of the specific elastic energy, specific dissipated energy, relative dissipated energy and rotation sensitive parameter $\gamma = \sqrt{\gamma_x^2 + \gamma_y^2}$, where $\gamma \rightarrow (\gamma_x, \gamma_y, \gamma_z)$ is the cumulative angle of material local rotation at the front faces of specimens with U-, V- and I-shaped notches at different temperatures (213 K, 253 K, 293 K) in 100 μ s after the beginning of loading.

The $\gamma = \sqrt{\gamma_x^2 + \gamma_y^2}$ value is responsible for the rotation perpendicular to the front face parallel to the coordinate plane XOY.



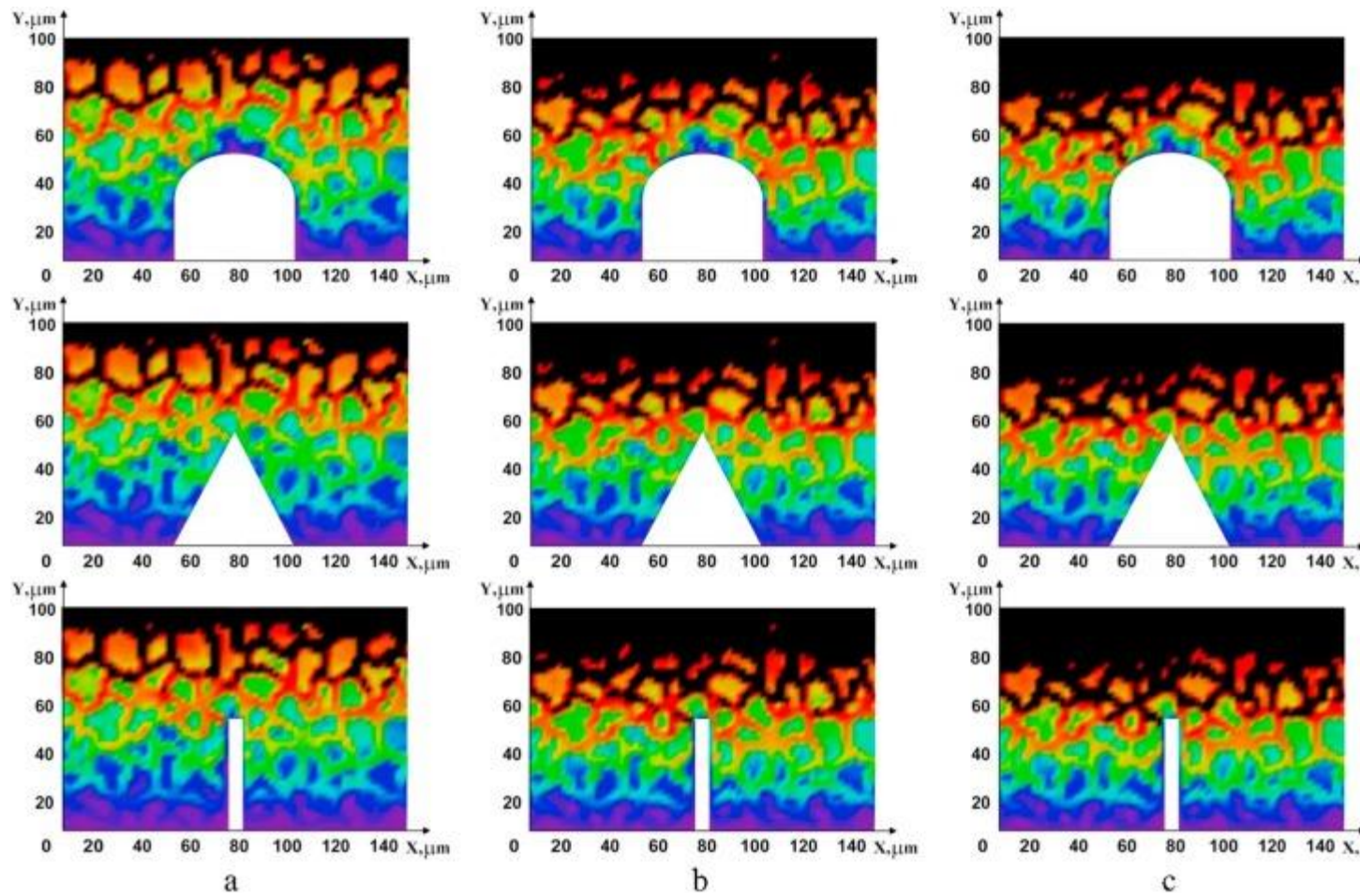
1. [Download high-res image \(218KB\)](#)
2. [Download full-size image](#)

Fig. 14. Distribution of the specific elastic energy at the front faces of specimens with U-, V- and I-shaped notches at different temperatures in $t = 100 \mu\text{s}$ after the beginning of loading: (a) 213 K; (b) 253 K; and (c) 293 K.



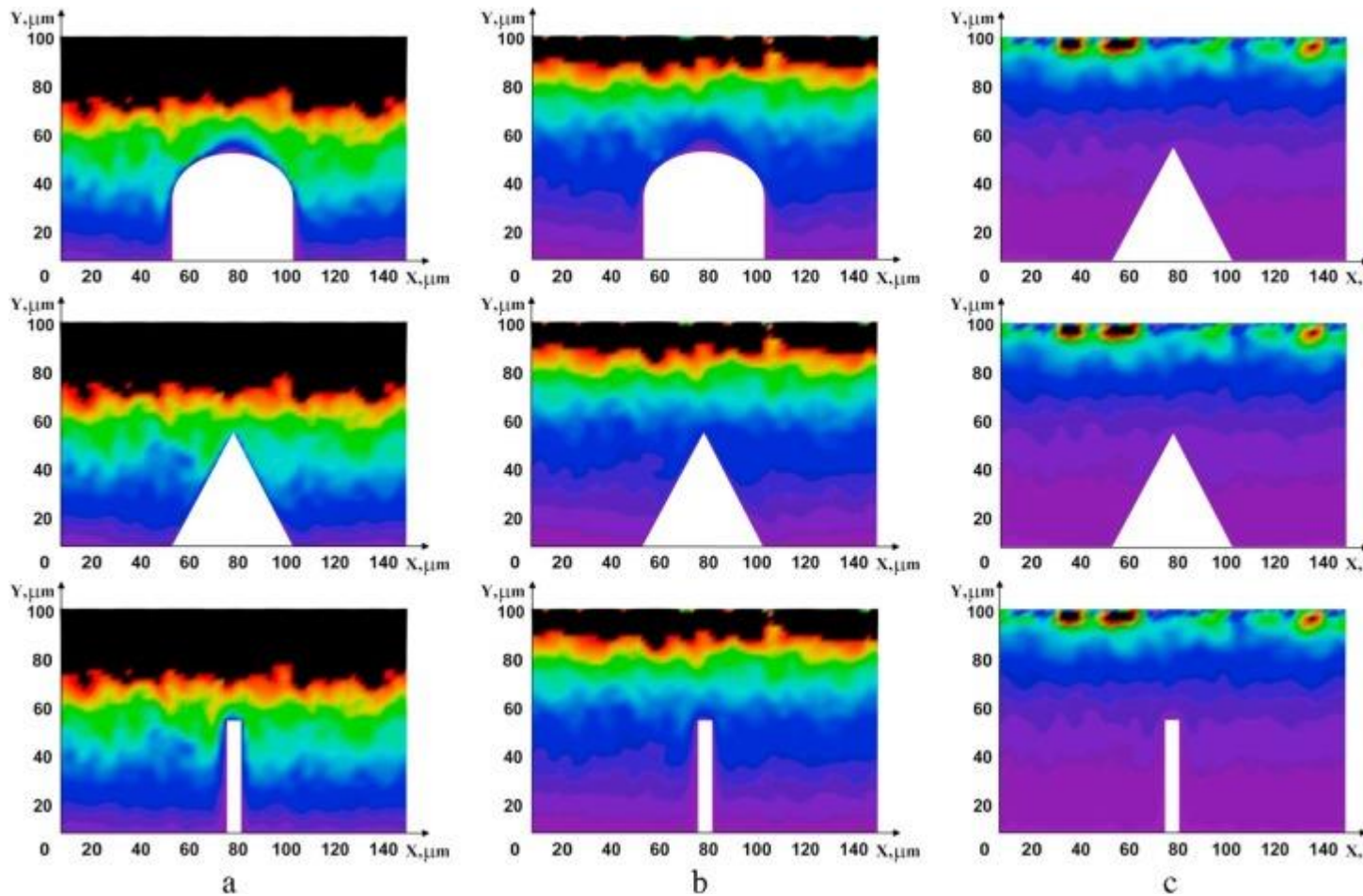
1. [Download high-res image \(324KB\)](#)
2. [Download full-size image](#)

Fig. 15. Distribution of the specific [dissipated energy](#) at the front faces of specimens with U-, V- and I-shaped notches at different temperatures in $t = 100 \mu\text{s}$ after the beginning of loading: (a) 213 K; (b) 253 K; and (c) 293 K.



1. [Download high-res image \(378KB\)](#)
2. [Download full-size image](#)

Fig. 16. Distribution of relative [dissipated energy](#) at the front faces of specimens with U-, V- and I-shaped notches at different temperatures in $t = 100 \mu\text{s}$ after the beginning of loading: (a) 213 K; (b) 253 K; and (c) 293 K.



1. [Download high-res image \(261KB\)](#)
2. [Download full-size image](#)

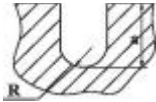
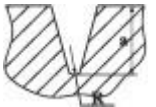
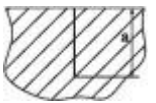
Fig. 17. Distribution of angular $\gamma = \gamma_x^2 + \gamma_y^2$ values at the front faces of specimens with U-, V- and I-shaped notches at different temperatures in $t = 100 \mu\text{s}$ after the beginning of loading: (a) 213 K; (b) 253 K; and (c) 293 K.

The [spatial distributions](#) of the main values analysed in the course of the [present investigation](#) shown in [Fig. 14](#), [Fig. 15](#), [Fig. 16](#), [Fig. 17](#) provide a vivid illustration of all the forgoing speculations. [Fig. 14](#) illustrates the increase of the elastic energy level with [decreasing temperatures](#). Comparison of [Fig. 15](#), [Fig. 16](#) prompts a conclusion about the accommodative nature of defect generation at the grain boundaries. The distribution of the cumulative rotation angle shown in [Fig. 17](#) is indicative of greater [micro-scale surface deformation](#) and greater probability of crack nucleation.

4. Experimental study of stage I (crack nucleation) impact loading of the 17Mn1Si steel

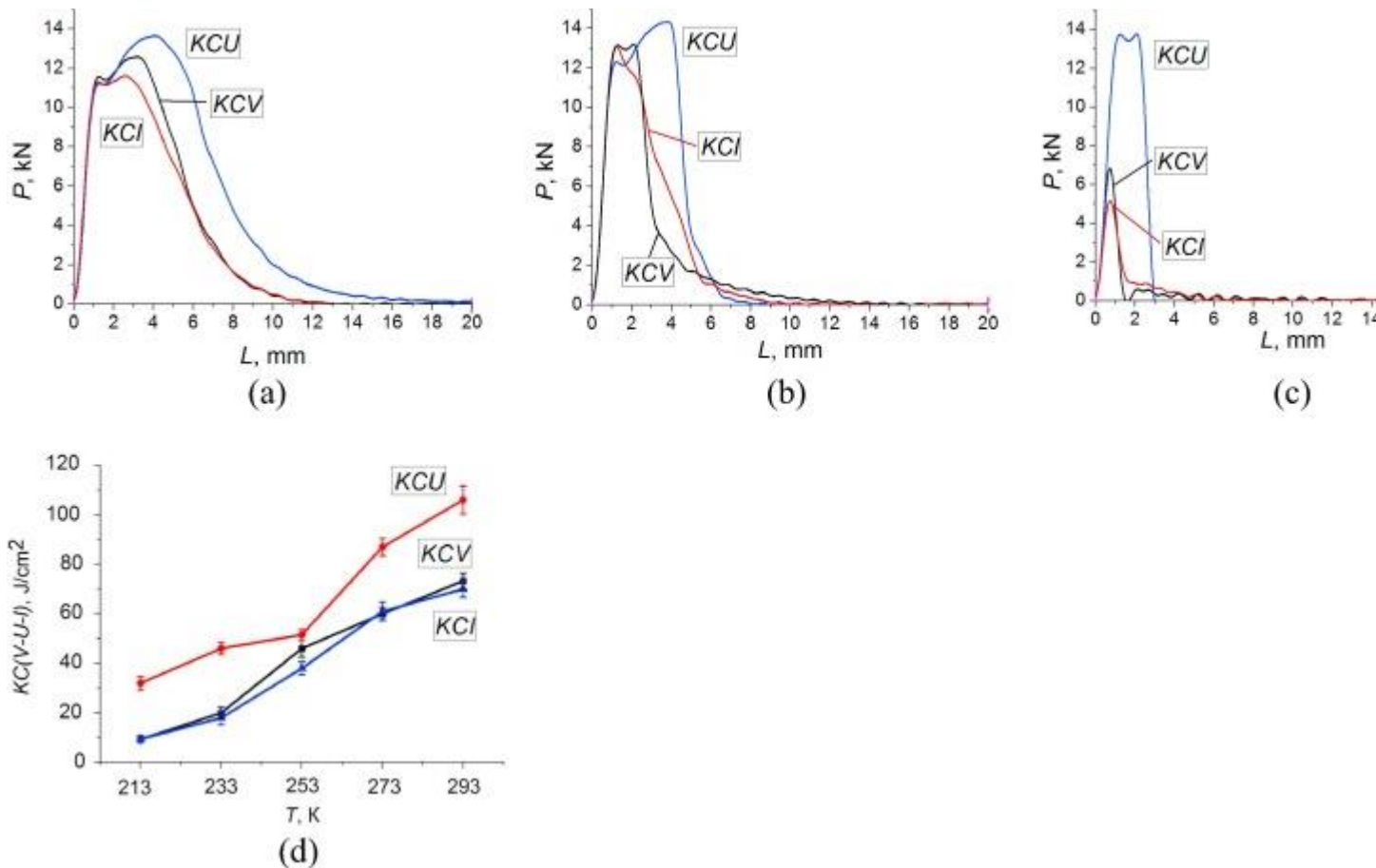
[Test specimens](#) were cut by spark erosion from the commercial 30 mm thick [rolled sheet](#). The specimens with V-, U- and I-shaped notches with equal length of 2 mm were machined. The V- and U-notches were induced by standard [milling cutters](#), while the I-shaped notch was made by electro erosion. Before [low-temperature impact loading](#), the specimens were kept in the refrigerator (cooling chamber “Lauda rp870”) for 10 min at temperatures of 213 K and 253 K. They were then quickly mounted into the grips of the instrumented impact [pendulum](#) Instron 450MPX for testing. The time interval between specimen extraction from the cooling chamber and further testing did not exceed 5 s. At least three specimens of each type were tested at each temperature. The tests were performed at 293, 253, and 213 K. The test summary is given in [Table 1](#). The [deformation](#) and [fracture mechanisms](#) were clarified post mortem by the fractographic analysis of fractured surfaces using a [scanning electron microscope](#) LEO EVO 50 (Zeiss, Germany).

Table 1. [Impact test](#) conditions for 17Mn1Si steel specimens.

Shape of notch	Geometric shape	Notch tip radius, R , mm	Notch length, a , mm
U-shaped		1.0	2.0
V-shaped		0.25	2.0
I-shaped		0.1	2.0

4.1. Macro-scopic features of fracture

According to the [temperature dependence](#) of [impact toughness](#) ([Fig.18d](#)), three characteristic types of the specimen response under impact loading can be distinguished [\[53\]](#). At lower temperature ($T = 213$ K) the specimen fracture is brittle with no visible evidence of [plastic deformation](#). Raising the [testing temperature](#) to 253 K results in a mixed fracture appearance. Room temperature $T = 293$ K testing gives rise to [ductile fracture](#), which is characterized by the intensive [plastic flow](#) at both [micro-](#) and [macro-levels](#). Apparently, different microscopic fracture mechanisms are relevant to each of these cases as has been frequently reported in the literature [\[54\]](#), [\[39\]](#).



1. [Download high-res image \(315KB\)](#)
2. [Download full-size image](#)

Fig. 18. [Impact loading](#) diagrams in “load-displacement“ coordinates for the specimens with different notch shapes at test temperature: 293 K (a); 253 K (b); 213 K (c); and [temperature dependence](#) of [impact toughness](#) (d).

It should be noted that the shape of the obtained impact toughness diagrams, [Fig. 18](#), for specimens with sharp V- and I-shaped notches (KCV and KCI, respectively) is practically identical for all testing temperatures. Some difference is seen at 253 K, where the impact toughness of specimens with V-notch is slightly higher than for the specimens with I-shaped one. A common finding is that throughout the whole test temperature range the impact toughness of specimens with U-shaped notch (KCU) is about 3 times higher than that for V-notch specimens. With a crude approximation, we can assume that the value of impact toughness of all three notch specimens decreases linearly with decreasing test temperature, [Fig.18d](#).

The obtained diagrams of [dynamic deformation](#) verify the specimen’s sensitivity to [changing conditions](#) of macro-scopic fracture [localization](#) related to the change in

the [concentrator](#) geometry, [Fig. 18](#). On the whole, it may be regarded as that typical of ductile fracture [\[55\]](#) for all tested temperatures from 293 K to 213 K for the specimens with sharper V- and I-notches. The apparent similarity of the impact fracture diagrams is indicative of the similarity of underlying mechanisms and stages [of crack initiation](#) and growth. Let us examine these in more detail for the specimens with different geometries.

4.1.1. V–notch

At test temperatures from 293 K to 253 K, the 17Mn1Si steel specimens undergo ductile fracture, which is suggested by quite low-sloped ascending and descending parts of the diagram, [Fig. 18](#) a and b, curve *KCV*. The [deformation mechanisms](#) on the micro-level provide a rather effective [stress relaxation](#) [\[56\]](#). The process of crack nucleation and growth occurs steadily, with no [disruption](#) or sharp bifurcation transitions. The material has a sufficiently high ductility and [crack resistance](#). At 213 K, narrowing of the fracture diagram is observed, its peak becomes a “pike-shaped“. The diagram descending tail shape suggests quite a brittle character of crack growth [\[56\]](#), [\[57\]](#). Note that at $T = 213$ K the maximum load is reduced to $P_{\max} = 7$ kN, which indicates a [partial loss](#) of the load [bearing capacity](#) of the material [\[58\]](#).

4.1.2. I–notch

The loading diagram shown in [Fig. 18](#)a–c, curve *KCI*, is similar in shape to that for the V–notched specimen, [Fig. 18](#)a–c. Thus, in the case of a most sharp concentrator, the [fracture behaviour](#) of the material does not become much more brittle. This is can be associated with the development of plastic deformation ahead of the propagating [main crack](#), providing thereby an efficient partial relaxation of the stress in the tested steel.

The influence of decreased temperature on the dynamic deformation and fracture behaviour of the specimens with this type of notch is similar to that for the V-shaped notch specimens. At $T = 213$ K, the value of the maximum [load reduces](#) even more steeply to $P_{\max} = 5$ kN, which is indicative of a more pronounced notch [embrittlement](#) effect, which is well aligned with its minimum tip radius.

4.1.3. U–notch

The impact fracture of 17Mn1Si steel specimens with the notch having maximum tip radius is accompanied by considerable plastic deformation. The observed pattern of the macroscopic [deformation behaviour](#) of the material indicates the activation of [relaxation processes](#) accompanied by the increased height and width of the impact deformation diagram within the entire investigated temperature range.

At room temperature, [Fig. 18a](#), the maximum load value decreases with the increase of [stress concentration](#) at the [notch tip](#). In so doing the height of the sharp yield point increases; such sharp yield point tip in the specimen with I-shaped notch corresponds to the maximum load P_{max} . Thus, the increase in the volume of material involved in the [deformation resistance](#) (c.f. the case of the U-shaped notch having larger area and larger radius) results in the delayed macro-crack nucleation and slower [crack propagation](#). However, this occurs at somewhat smaller values of load P at the stage of [elastic deformation](#) if compared to the I-notched specimen.

The yield plateau is not well marked in the impact loading diagrams for the I-notch specimen. It witnesses about the development of local [hardening processes](#) on the early deformation stages accompanied by the decrease of steel resistance to localization of flexural strain (which is very dangerous for pipeline facilities).

4.2. Integral estimations of impact loading diagram

From the perspective of application of experimental data in fracture modelling, it is of acute importance to determine the moment of transition from stable to [unstable crack growth](#). [Table 2](#), [Table 3](#) summarize the force and energy parameters of [fracture toughness](#) of the 17Mn1Si steel. Similar to our earlier reported results, the maximum load P_{max} in [impact tests](#) can be deemed to be a macro-scopic characteristic reflecting the dynamic strength of the material.

Table 2. Maximum load values in the [impact load](#) diagram.

<i>T</i>, K	<i>P</i>_{max}, kN		
	V-shaped notch	U-shaped notch	I-shaped notch
213	6.8 ± 0.2	13.8 ± 1.7	5.2 ± 0.1
253	13.2 ± 1.01	14.3 ± 0.6	13.1 ± 1.3
293	12.6 ± 2.3	13.7 ± 1.3	11.6 ± 1.5

Table 3. Energy of crack nucleation in steel 17Mn1Si specimen at impact bending with different notch shapes.

<i>T</i>, K	The energy of crack initiation, <i>A</i>_i, J		
	V-shaped notch	U-shaped notch	I-shaped notch
213	2.47	20.22	2.06
253	18.31	38.76	7.65
293	27.37	37.55	21.13

These data are important from the standpoint of the stress state stiffness effect on the resistance of 17Mn1Si steel to crack propagation, as P_{max} corresponds to the moment of

transition from nucleation to propagation of a macro-crack. There is an indication that with a sharper concentrator the crack growth occurs at a lower value of P_{max} suggesting a more rigid stress state at the [crack tip](#) [59], [60].

Moreover, the total energy of [Charpy](#) specimen fracture (A_t) consists of two [main components](#) – the energy of [crack initiation](#) (A_i) and the energy of its propagation (A_p), [Table 3](#). The data on crack initiation (nucleation) work is represented below for comparison against the [numerical simulation](#) findings.

The data shown in [Table 3](#) that summarizes the crack initiation energy for various testing temperatures and notch shapes agrees well with results shown in graphs of [Fig. 10a](#). This is manifested in the fact that the sharper the notch the [higher level](#) of [energy dissipation](#) is achieved in its tip due to [deformation processes](#) development. It is this reason why in the [numerical calculations](#) at the onset of dynamic [compression stage](#) at $t = 100 \mu s$ and ambient testing temperature the highest dissipation takes place in U-notched specimen. At the lowest testing temperature $T = -60^\circ C$ the difference in the value of the parameter under analysis becomes negligible due to suppression [in running](#) dissipation processes. Also, it is this reason why at the lowest impact bending temperature for the two more [sharp notches](#) the impact toughness is close to zero while for the bluntest U-shape one it is somehow higher. One more [numerical experiment](#) result worth mentioning and discussion is revealed possibility of deformation process development at the unloading stage (tensile part of the dynamic impact). For sure, the impact pendulum testing does allow to conduct such analysis since it is aimed at specimen fracture only. [Fig. 12c](#) shows that at the loading time $t = 900 \mu s$ the average angle velocity degree at [grain boundaries](#) possesses the maximum value exactly at the lowest temperature $T = -60^\circ C$. This means that the energy accumulated at grain boundaries at the previous loading stage (dynamic compression) is released during the unloading (dynamic tension). In doing so it is highly manifested at lowest dissipation ability of internal structure elements.

Quite important interpretation of numerical simulation results on specific [elastic energy](#) estimation ([Fig. 9](#)) might be given at its comparison with shown below in [Table 5](#) and [Fig. 22](#), [Fig. 23](#), [Fig. 24](#) data on energy released at the first stage of impact fracture (crack initiation stage). It is seen that with increasing the temperature of the dynamic compression the value of the specific elastic energy gradually decreases that might be easily explained at the account of intensification of [dissipative processes](#) development within [structural elements](#) of [polycrystalline](#) aggregate. From the other hand, the part of the energy released at the crack initiation is increased with the temperature that testifies for the fact that the [energy absorbed](#) onto impact

Sharpy [specimen failure](#) (besides transformation into heat one) is expelled in the form of [elastic waves](#) being registered by [piezoelectric sensors](#) of [acoustic emission](#).

Table 5. Expended [mechanical energy](#) E_{exp} and released acoustic energy E_{rel} at impact bending of 17Mn1Si steel at different temperatures.

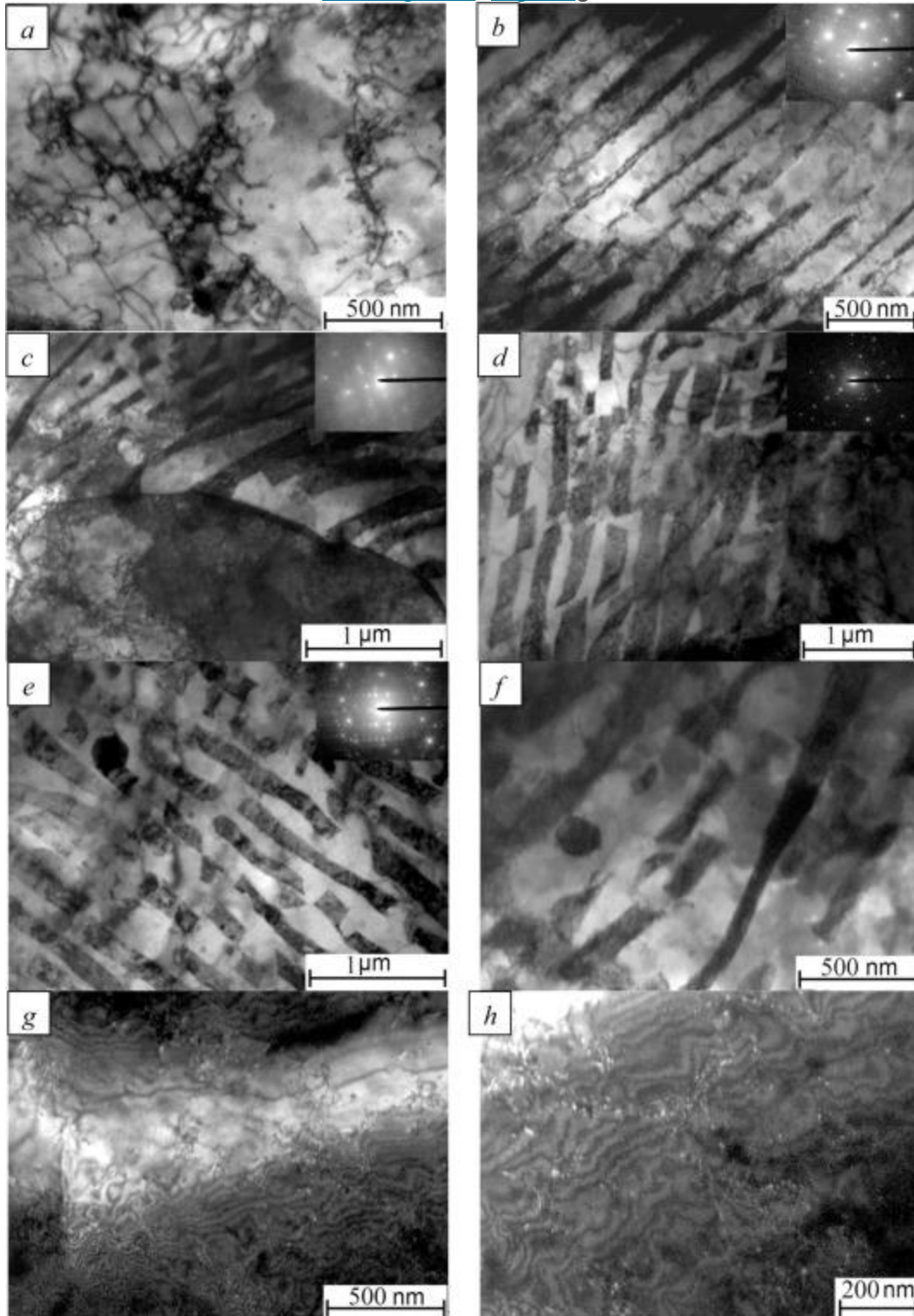
T, K	E_{exp}, J	$E_{rel}, a.u.$	E_{exp}, J	$E_{rel}, a.u.$	E_{exp}, J	$E_{rel}, a.u.$
	U-shaped		V-shaped		I-shaped	
293	37.55	0.403	27.37	0.136	21.13	0.046
253	38.76	0.098	18.31	0.077	7.65	0.031
213	20.22	0.072	2.47	0.046	2.06	0.027

For sure, total similarity between numerical calculations and laboratory experiments could not be achieved at least for the reason that the [model does](#) not takes into consideration development of fracture processes that are governing at impact [bending tests](#). However, in the framework of the used [problem statement](#) the authors do not aim at attaining the complete similarity. However, the problem of illustrating the important role of energy dissipation at grain boundaries to our opinion is successfully solved. Moreover, the particular complexity of experimental studies of fast developing processes to take place at the [mesoscale](#) level should be pointed out. Sometimes they even possess bifurcation pattern of their development. Within the framework of the current [study computer simulation](#) does not completely imitate the experiments but complements it. In the current research through running numerical experiment we attempt to calculate [energetic](#) parameters of the mesovolume in the [local region](#) where [primary crack](#) is going to nucleate at the onset of its opening. In doing so the duration of the energy redistribution process under simulation did not exceed 1 μs . To our opinion the detailed simulation of such processes is of particular importance with the view of interpretation of experimentally attained data.

5. Crack nucleation mechanisms. Crack initiation region investigation (Area I)

It should be noted that the [crack initiation](#) work under [impact loading](#) is directly related to generic types of [microstructures](#) and the specific dislocation structure formed during thermomechanical processing at the [manufacturing stage](#). The 17Mn1Si steel has a typical ferrite-pearlite structure, [Fig. 19a–c](#). In pearlite, [cementite](#) plates are typically of 100–250 nm thick. Fragmented plates of cementite, which are frequently seen in the [microstructure](#), are formed in the course of [hot rolling](#), [Fig. 19d](#) and [e](#). Besides the layered cementite plates, some amount of a globular cementite phase can be

found, [Fig. 19e](#) and [f](#). Fine cementite particles of 10–24 nm are observed near dislocation bundles in the [ferrite grains](#), [Fig. 19g](#) and [h](#).



1. [Download high-res image \(626KB\)](#)
2. [Download full-size image](#)

Fig. 19. TEM-microphotographs of the 17Mn1Si [steel microstructure](#).

The [transmission electron microscopy](#) images, [Fig. 19a–h](#), show the morphology of the cementite plates in the [ferritic matrix](#) of 17Mn1Si steel. Thus, at the [micro-level](#), the [steel structure](#) is a “composite”-like one, where ductile layers alternate with brittle compounds. When the crack starts (at 293 K), it sprouts through zones with a pronounced gradient of properties, which stimulates the high [impact strength](#) of 17Mn1Si steel demonstrating relatively low plasticity. At lower testing temperatures, the effect of this structural heterogeneity is diminished, since the plasticity of the [ferrite](#) decreases. However, at the stage of [crack growth](#), when a [short crack](#) turns into a long one (the length of the latter is much larger than the size of structural elements), this factor becomes of less importance.

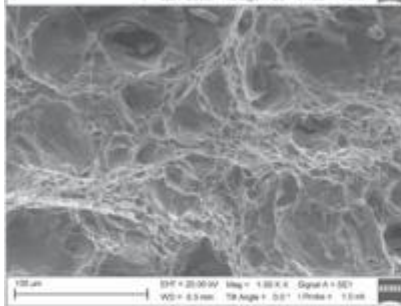
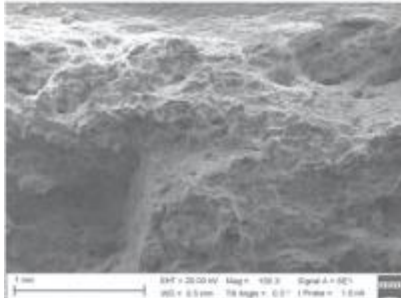
The work required for crack initiation under impact loading is determined by the volume and the value of [plastic deformation](#) at the [notch tip](#), specifically at the crack initiation site. Also, as demonstrated above, the [testing temperature](#) reduction leads to decreasing materials [deformability](#). This is particularly pronounced near the notch, where the temperature reduction results in a drop of the work required for crack initiation due to impeded plastic deformation, which is reflected in the microscopic [fracture mechanisms](#).

To identify the role of microstructural elements of a ferritic-pearlitic steel in resistance to impact fracture, a fractographic analysis of specimen [fracture surfaces](#) was undertaken. Besides, this analysis helped to reveal the features of prevailing fracture mechanisms.

5.1. T = 293 K

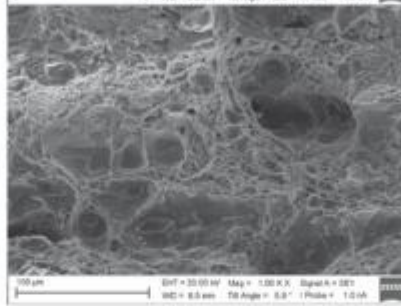
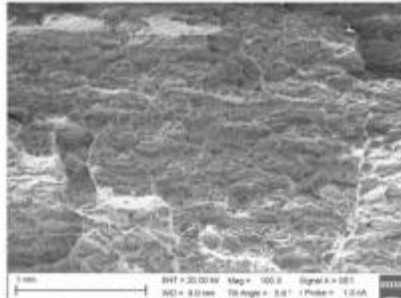
Fracture at this temperature is characterized by significant plastic deformation as is evidenced by well-developed ductile dimples on the fracture surface. Since the formation of voids requires a large amount of plastic energy, the observed fracture surface illustrates the high deformability of the material at this temperature. The surface at the crack initiation site shows the typical features of [ductile fracture](#). In particular, the dimples, which are formed by [delamination](#) of dispersed inclusions in the ferritic matrix, are clearly seen in [Fig. 20a–c](#). Characteristic [macroscopic](#) dimples surrounded by conglomerates of smaller dimples are also frequent. Despite some difference in shapes and sizes, the overall [physical nature](#) of dimple formation is similar for all specimens with different notches.

V



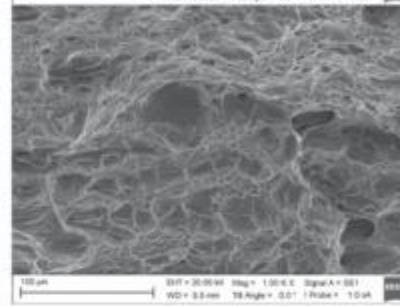
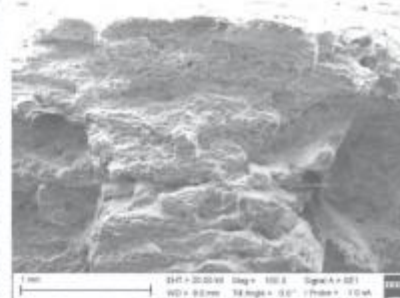
(a)

I

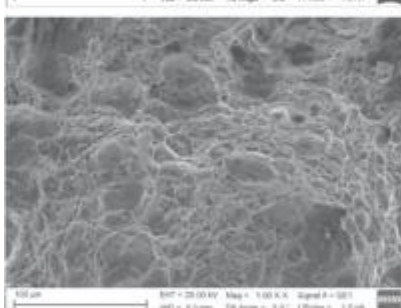
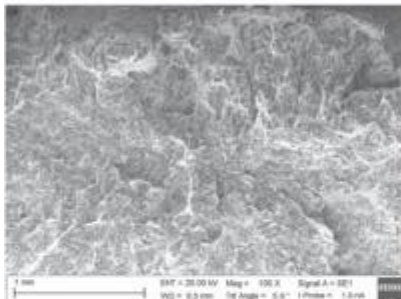


(b)

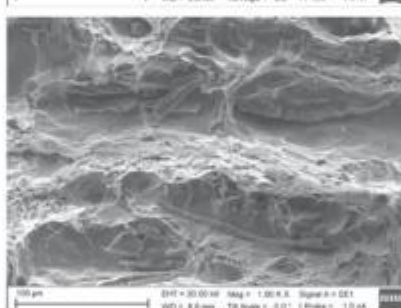
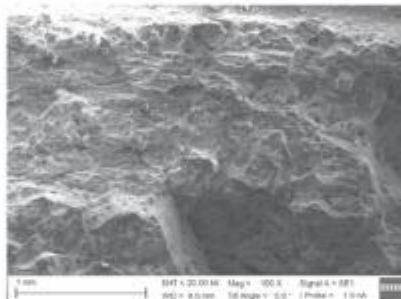
U



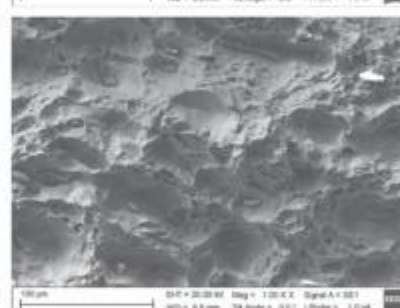
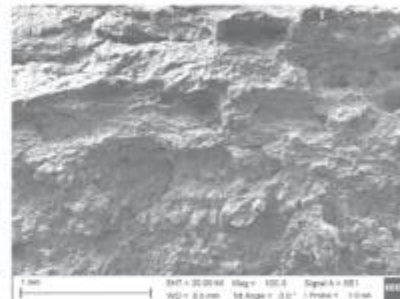
(c)



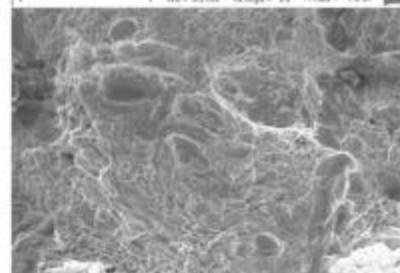
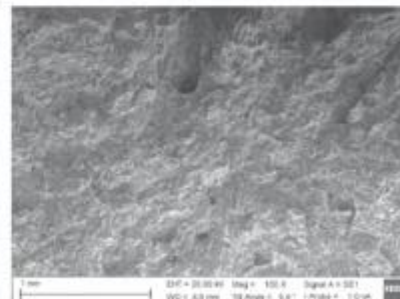
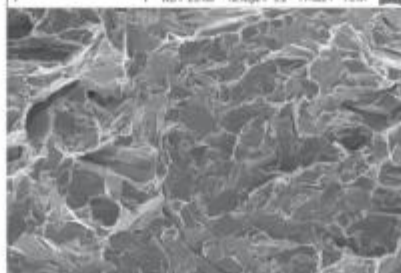
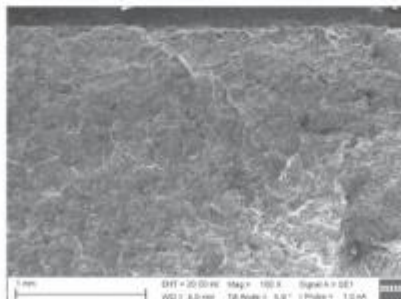
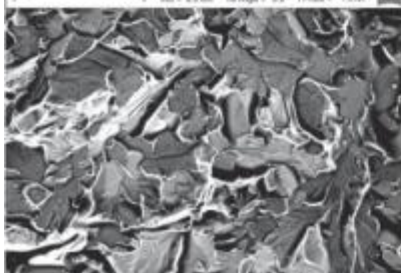
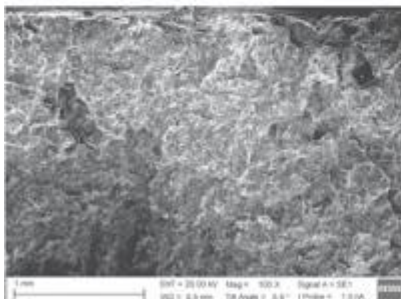
(d)



(e)



(f)



1. [Download high-res image \(2MB\)](#)
2. [Download full-size image](#)

Fig. 20. SEM [micrographs](#) of the [fracture surface of crack initiation](#) region in the specimens with different notch geometries tested in impact bending at different temperatures (a–c) 293 K; (d–f) 253 K; and (i–l) 213 K.

5.2. T = 253 K

Lowering the testing temperature resulted in the decrease of [material ductility](#). The [fracture toughness](#) compromised therefore too. This drop in ductility significantly affected the morphology of the fracture surface. The regions of mixed quasi-cleavage fracture appeared along the [crack path](#). On the other hand, the material still retains some ductility, which is seen in the dimpled areas of the fracture surface. Besides, significant curvature of the [crack front](#) may be indicative of microscopically non-uniform [crack propagation](#) due to interaction of the crack front with [grain boundaries](#). A number of differences were identified with regard to fracture mechanisms:

-

- for the specimens with V–notch, the fracture mechanism is similar to that at $T = 293$ K. Some reduction in ductile dimple size can be noticed, [Fig. 20d](#).

-

- for the specimens with U–notch, the fracture surface is featured by delamination of large [non-metallic inclusions](#) serving as seeds for dimples.

-

- for the specimens with I–notch, the fracture surface relief is characterized by brittle (or quasi-brittle) faceted relief, [Fig. 20f](#), as well as by some regions with ductile microscopic relief.

5.3. T = 213 K

Grain boundaries at this temperature are not able to adapt themselves to the rapidly [increasing stresses](#) during impact load. The lattice and grain boundary defects such as dislocations and disclinations accommodate some [plastic strains](#) but act as microscopic local [stress risers](#) promoting quasi-brittle intercrystalline fracture. Cleavage and quasi-cleavage were identified as primary mechanisms of fracture at this temperature. The facet size increased as compared to the facets observed at 253 K. A number of [characteristic fracture](#) features at this temperature can be distinguished as follows:

-

for the specimens with V–notch, the fracture surface exhibits a characteristic river pattern, [Fig. 20 i](#). It is covered with cleavage ridges formed by merging micro-cracks on parallel regions under concurrent plastic deformation.

•
for the specimens with U–notch, the fracture is of mixed type, [Fig. 20k](#). Clearly, the primary mechanism is cleavage. Concurrently, some [shallow](#) micro-dimples are observed on the fracture surface. Superposition of these mechanisms gives the fracture surface a very disordered appearance.

•
for the specimens with I–notch, the quasi-cleavage occurs during [dynamic fracture](#), [Fig. 20l](#), that is characterized by [brittle fracture](#) after accumulating some plastic deformation. As a result, regions with brittle fracture facets are surrounded by ductile micro-dimpled areas.

Identified surface fracture patterns produced by [initiated crack](#) in the 17Mn1Si steel under impact loading in different temperature-force conditions are summarized in [Table 4](#).

Table 4. Microscopic mechanisms of fracture of 17Mn1Si steel under impact bending with different notch shapes.

<i>T</i> , <i>K</i>	Morphological components of the fracture surface		
	V-shaped notch	U-shaped notch	I-shaped notch
213	Cleavage facets (river pattern)	Cleavage facets + shallow micro-dimples	Cleavage facets + micro-dimples
253	Ductile dimples (small, round micro-dimples)	Delamination (delamination at inclusions)	Ductile dimples (with flat bottom) + cleavage facets
293	Ductile dimples (round shape)	Ductile dimples (round shape)	Ductile dimples (round shape)

6. Analysis of acoustic emission signals during impact bending of specimens at different temperatures

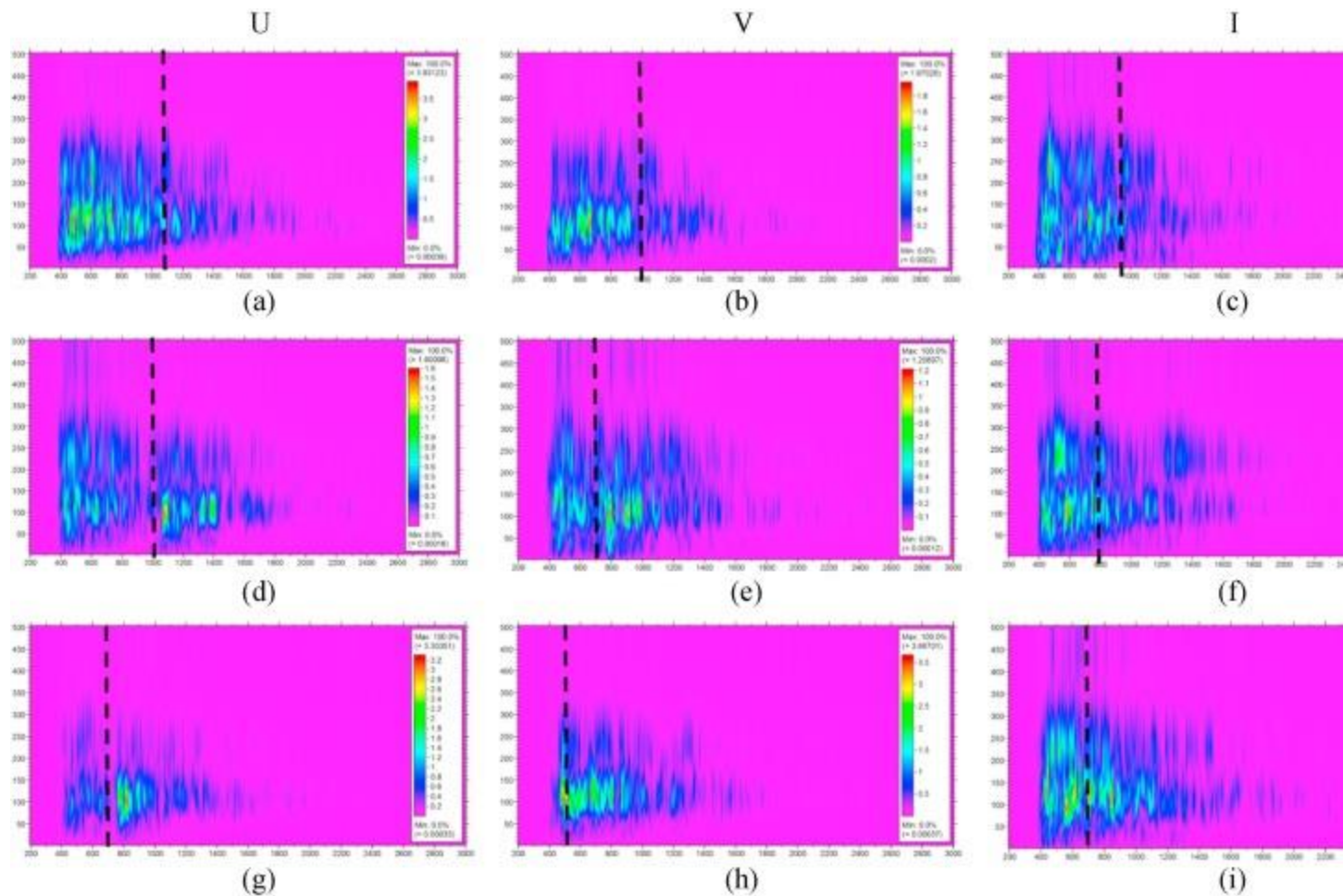
In the course of [impact testing](#), an [acoustic emission](#) (AE) signal induced by fracture was recorded. For that purpose, a wide band AE [transducer](#) (WD, Physical Acoustics) was mounted on the bed of the [pendulum](#) of 0.5 m apart from the specimen position. The distant [sensor location](#) caused some attenuation of the elastic acoustic waves thus allowing to exclude overshooting in the electric signal at the sensor output after impact. Due to the high [amplitude](#) of the [recorded signal](#), the AE transducer was connected directly to the ADC board PCI-9812 (Adlink) operating with the [sampling rate](#) of 10 MHz at ± 1 V [input voltage](#) range. The [high value](#) of the [sampling frequency](#) was taken to

increase time resolution since the impact fracture is fast running process. The frequency filtration was conducted regarding the [operating band](#) of AE transducer.

The Garbor continuous wavelet spectra were calculated using the free “AGU-Vallen Wavelet” software [60]. The range of frequencies (frequency band) investigated was from 50 to 500 kHz with a step of 5 kHz. To calculate the energy of the detected acoustic signals, they were normalized to unity by the maximum value found among all notch shapes and [testing temperatures](#) for comparison. The global maximum value corresponded to U-shaped notch failed at $T = 293$ K. This makes it possible to adequately compare the results obtained at variation of [testing conditions](#). The envelope of the acoustic signal recorded at impact fracture, was smoothed by the *lowess* filter with the 20 μ s time window size.

The obtained results can be interpreted in terms of brittle vs. [ductile fracture](#), considering the effect of the notch shape and testing temperature on the magnitude of the expended [elastic energy](#) (by using the loading diagram) and released elastic energy (by using the AE data).

[Fig. 21](#) displays the wavelet time-frequency distributions of AE signals recorded during testing the specimens with different notch shapes at various temperatures: $T = 293$ K (a–c), $T = 253$ K (d–f), $T = 213$ K (g–i). The dotted line in all spectra indicates the boundary that separates the stages [of crack initiation](#) (I) and propagation (II). Even a superficial juxtaposition of the represented data demonstrates that with [decreasing temperature](#) and, consequently, increasing area of [brittle fracture](#), the major fraction of the released [energy shifts](#) to stage II. This shift is observed virtually regardless of the notch shape. This trend is seen clearly for the specimens with the bluntest U-shaped notch, [Fig. 21](#)a, d, and g. On the other hand, in the case of the sharpest I-notch, the AE spectrum appearance changes to a much [lesser extent](#) at all three testing temperatures, [Fig. 21](#)c, f, and i. This is most likely due to the fact that with the low work of fracture and with the brittle character of the macro-crack, the release of elastic (acoustic) energy due to [crack propagation](#) is higher than that at the nucleation stage (when [crack initiation](#) is accompanied by [energy dissipation](#) due to intensive [plastic deformation](#) at the notch tip).



1. [Download high-res image \(684KB\)](#)
2. [Download full-size image](#)

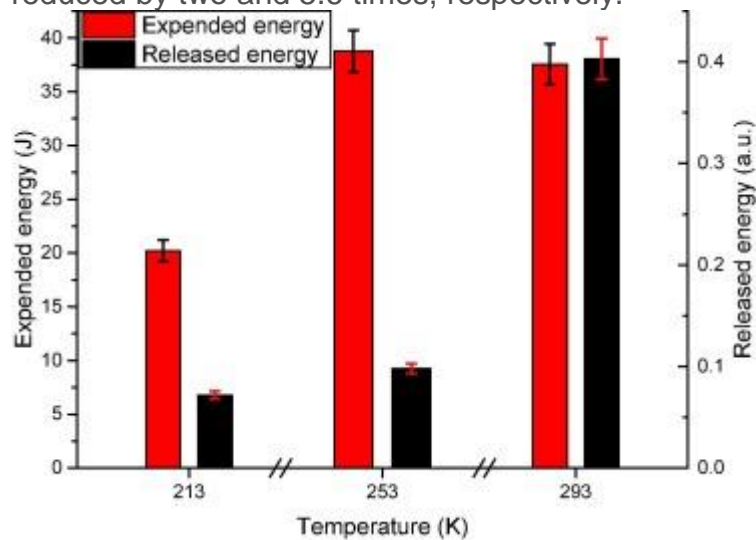
Fig. 21. Time-frequency distribution of the AE energy during testing of specimens with different notch shapes at 293 K (a–c), 253 K (d–f), and 213 K (g–i).

In the next step of data analysis, we compared [fracture energies](#) derived from the impact fracture diagrams and independently from the AE data. Each data set was divided into two stages and the first stage corresponding to crack nucleation was taken into account under the analysis. The values of expanded and released energy at the second impact bending stage were also analysed in the study. However, we confined ourselves to the early stages in this work and [numerical simulations](#) of crack propagation are not the part of the model, these data are not included in this paper. The fracture energy determined from the impact bending diagram (expanded energy E_{exp}) was plotted in [Joules](#), and the one evaluated from the acoustic signal analysis (released energy E_{rel}) was represented in arbitrary units (a.u.). Their comparison and the analysis for the specimens with different notch shapes is provided below. Data for all types of

specimens and testing temperatures are summarized in [Table 5](#). Let us consider in brief the results obtained for the specimens with different notch geometries.

6.1. U-shaped notch

[Fig. 22](#) shows that as the temperature decreases the energy of crack nucleation in the U-notch specimen exhibits initial slight grows from $E_{\text{exp}1} = 37.6 \text{ J}$ at $T = 293 \text{ K}$ to $E_{\text{exp}2} \sim 38.8 \text{ J}$ at $T = 293 \text{ K}$. It then decreases to $E_{\text{exp}3} \sim 20.2 \text{ J}$ at $T = 213 \text{ K}$ as is reasonably anticipated. Earlier this energy reduction was associated with the increasing brittle area fraction. Thus, the temperature decrease by $\Delta T = 80 \text{ K}$ is accompanied by only a twofold reduction in the crack initiation energy. From the perspective of the released fracture energy evaluated from AE data, the consistent trend is observed: the AE energy reduces gradually with temperature from $E_{\text{rel}1} = 0.403 \text{ a.u.}$ to $E_{\text{rel}2} \sim 0.098 \text{ a.u.}$, and further to $E_{\text{rel}3} \sim 0.072 \text{ a.u.}$ (i.e. about fivefold decrease). Thus, at the stage of macro-crack nucleation, when the effect of energy dissipation processes, which take place at the internal elements of the [microstructure](#) (including grain boundaries), is crucial, and under conditions of the most ductile fracture the expended and the released fracture energies reduced by two and 5.6 times, respectively.

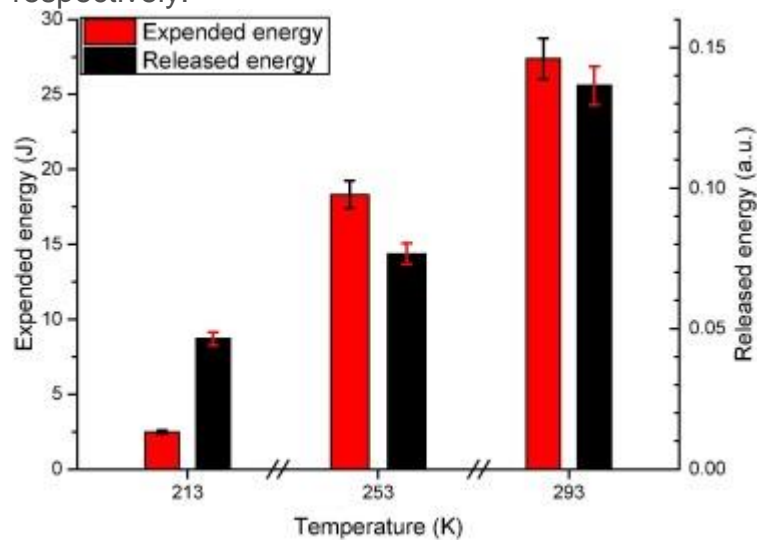


1. [Download high-res image \(120KB\)](#)
2. [Download full-size image](#)

Fig. 22. The crack [nucleation energy](#) computed using the loading diagram (black bars) and AE data (red bars) for the specimens with U-notch at different temperatures 293 K; 253 K; and 213 K. (For interpretation of the references to colour in this figure legend, the reader is referred to the web version of this article.)

6.2. V-shaped notch

For sharper V-notch the fraction of the crack nucleation [expended energy](#) is less as compared to that in the specimens with U-shaped notch. As the temperature decreases, this energy reduces much faster: $E_{\text{exp } 1} \sim 27 \text{ J}$; $E_{\text{exp } 2} \sim 18 \text{ J}$ and $E_{\text{exp } 3} \sim 2 \text{ J}$, [Fig. 23](#). The trend for the released energy assessed by the AE method looks similar: $E_{\text{rel } 1} \sim 0.136 \text{ a.u.}$; $E_{\text{rel } 2} \sim 0.077 \text{ a.u.}$; $E_{\text{rel } 3} \sim 0.046 \text{ a.u.}$. The fraction of the energy expended at the crack nucleation stage dropped most dramatically at the lowest temperature $T = 213 \text{ K}$. Thus, the increase of the [stress concentration factor](#) at the [notch tip](#) of [Charpy](#) specimens is accompanied by a more pronounced decrease in the crack [nucleation energy](#) compared to that in the U-notched specimens. The expended and the released fracture energies reduced by about fourteen times and three times, respectively.



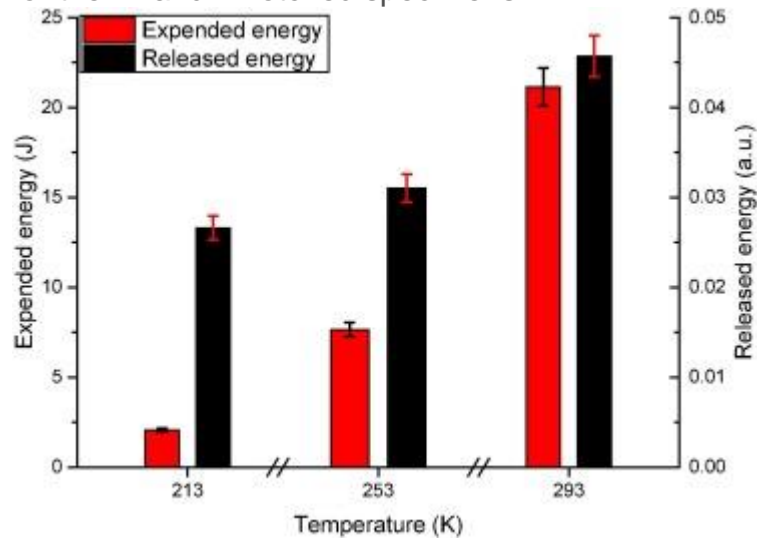
1. [Download high-res image \(116KB\)](#)
2. [Download full-size image](#)

Fig. 23. The crack [nucleation energy](#) computed using the loading diagram (black bars) and AE data (red bars) for the specimens with V-shaped notch at different temperatures 293 K; 253 K; and 213 K. (For interpretation of the references to colour in this figure legend, the reader is referred to the web version of this article.)

6.3. I-shaped notch

The data recorded during testing of the specimens with the I-shaped notch were organized in the same way as above, [Fig. 24](#). The trends in the energy changes with temperature resemble those for the above described specimens, particularly for the V-notched ones. The crack nucleation energy for the I-notched specimen decreases rapidly with decreasing temperature: $E_{\text{exp } 1} \sim 22 \text{ J}$; $E_{\text{exp } 2} \sim 8 \text{ J}$; $E_{\text{exp } 3} \sim 2 \text{ J}$, i.e. the energy reduces by a factor of 11 with temperature reduction. The similar trend is seen for the

released AE energy, however the change does not exceed a factor of 2. Thus, the overall behaviour of the expended [mechanical energy](#) and the released AE energy during Charpy specimen fracture at different temperatures are qualitatively very similar for the V- and I-notched specimens.



1. [Download high-res image \(118KB\)](#)
2. [Download full-size image](#)

Fig. 24. The crack [nucleation energy](#) computed using the loading diagram (black bars) and AE data (red bars) for the specimens with the I-shaped notch at different temperatures 293 K; 253 K; 213 K. (For interpretation of the references to colour in this figure legend, the reader is referred to the web version of this article.)

The analysis of the obtained results shows that at the stage of crack initiation, the AE energy consistently reduces in proportion to the decrease of the expended mechanical energy. One should bear in mind that from the standpoint of the energy expended to [initiation fracture](#), the role of the energy dissipation processes, which occur on the elements of the microstructure, is of particular importance on this stage. As established by some of the authors in similar studies [\[61\]](#), [\[62\]](#), [\[63\]](#), [\[64\]](#), these trends are reversed at the stage of crack propagation. Therefore, the important role of [energy release](#) at the interface/grain boundaries and its decreasing significance with decreasing temperature shown in numerical simulations described in the first part of the paper was also demonstrated in the course of experimental studies.

7. Summary and conclusions

Further to the development of the excitable cellular automata method, a model describing the [polycrystalline](#) aggregate behaviour under [impact loading](#) at different temperatures was proposed. The model specifically highlights the significance of [energy](#)

[dissipation](#) due to [local material](#) rotations. The change in the [mechanical energy](#) of each cellular automaton element determines the increment in the material rotation energy in the element in proportion to the [dissipation factor](#) being an increasing function of temperature. Further conclusions are categorized in regard to highlight particular importance of each key governing parameter.

7.1. Temperature \Leftrightarrow dissipative processes

The numerical analysis of the [deformation behaviour](#) at the [meso-scale](#) of modelled specimens with the structure and properties resembling those of the 17Mn1Si steel was performed at different [testing temperatures](#). A clear dependence on the enhancement intensity of [dissipative processes](#) with increasing the temperature was demonstrated together with the fundamental role played by those processes in [stress relaxation](#) at the boundaries of [structural elements](#) (grain and interface boundaries). The latter were clearly expressed in terms of specific [dissipated energy](#) and average [absolute value](#) of the [angular velocity](#) of local rotations.

7.2. Temperature \Leftrightarrow stress relaxation at grain boundaries

The [numerical simulation](#) of the deformation behaviour of model specimens, which was performed for different test temperatures, predicted a clear [temperature dependence](#) of the dissipative [deformation processes](#). The fundamental role played by those processes in stress relaxation at the boundaries of structural elements (grain and interface boundaries) was highlighted in this way.

7.3. Defect generation rate and rotation energy accumulation

It was established that under [dynamic loading conditions](#) the difference in the defect generation rate and rotation energy accumulation should be a [starting point](#) for formulation of the [crack opening](#) to be formulated. At equilibrium, the curl of all continuous displacements in the media must be zero which is not the case in structurally heterogeneous materials at each instant of time. It is however fulfilled on average over a certain time interval. Therefore, the curl of the material [rotation angle](#) increment in the selected meso-volume should be deemed a crack-opening criterion. In the future research, an adequate fracture model and [simulation algorithms](#) will be developed on the basis of such a criterion of [crack extension](#).

7.4. Temperature \Leftrightarrow notch shape

The testing temperature is found to be a more decisive factor for the [material behaviour](#) at the meso-level, than the notch shape and sharpness. The notch shape

determines the [materials response](#) on the [macro-scale](#), where the fraction of grain/interface boundaries is averaged over a large volume. Moreover, it is argued at the mesoscale level in the area adjacent to the stress [concentrator](#), the durations of processes of [elastic energy](#) accumulation and relaxation are dependent not only on the velocity of the elastic energy flow and material properties, but are also explicitly temperature dependent. Hence, at a mesoscale level, the fracture onset is driven by the energy state of the [grain boundaries](#), which strongly depends on temperature.

7.5. Temperature \Leftrightarrow impact toughness

The effect of temperature on the [impact toughness](#) of the 17Mn1Si steel was documented. The [fracture energy](#) characteristics of the 17Mn1Si steel were obtained from mechanical and independently measured [acoustic emission](#) data. The value of the impact toughness was demonstrated to be almost linearly decreasing with temperature, which was found consistent with the fractographic observations.

7.6. Temperature \Leftrightarrow energy release at grain boundaries

At the stage [of crack initiation](#), when the energy dissipation processes at the internal structure elements significantly affect the initiation of [dynamic fracture](#), the acoustic emission energy reduces in proportion to the expended mechanical energy, which, in turn, considerably decreases with temperature. An pretty agreement between the mechanical and acoustic emission energy measurements is found. Hence, the vital role of the [energy release](#) at interface/grain boundaries and its decreased significance with [decreasing temperature](#) is demonstrated both in numeric simulations and in dynamic experiments.